Intense hydrothermal scavenging of ^{230}Th and ^{231}Pa in the deep Southeast Pacific

Frank Pavia[a,b,*], Robert Anderson[a,b], Sebastian Vivancos[a,b], Martin Fleisher[a], Phoebe Lam[c], Yanbin Lu[d], Hai Cheng[d,e], Pu Zhang[d], R. Lawrence Edwards[d]

[a] Lamont-Doherty Earth Observatory of Columbia University, Palisades, NY, USA
[b] Department of Earth and Environmental Sciences, Columbia University, New York, NY, USA
[c] Department of Ocean Sciences, University of California, Santa Cruz, CA 95064, USA
[d] Department of Earth Sciences, University of Minnesota, Minneapolis, MN, USA
[e] Institute of Global Environmental Change, Xi'an Jiaotong University, Xi'an, China

ARTICLE INFO

ABSTRACT

Hydrothermal circulation and subsequent eruption of seawater at mid-ocean ridges and back-arc basins has great potential to modulate deep ocean biogeochemistry, acting as both a source and a sink for many trace elements and their isotopes. The influence of hydrothermal vents as a source of iron and manganese has been demonstrated in all ocean basins. However, the long-range impact of scavenging by hydrothermal particles has yet to be documented in detail. We use dissolved and particulate measurements of long-lived radiogenic (^{230}Th, ^{231}Pa) and primordial (^{232}Th) radionuclides to investigate the nature and geographic scale of scavenging processes occurring within a hydrothermal plume in the Southeast Pacific Ocean sampled during the GEOTRACES GP16 section. Due to their radioactive disequilibrium with respect to production by their parent uranium isotopes, ^{230}Th and ^{231}Pa provide unique insights into the rates of scavenging. We find strong deficits in ^{230}Th and ^{231}Pa coincident with elevated particulate Mn and Fe(OH)$_3$, indicating that trace metal scavenging is widespread and likely the result of the strong affinity of trace metals for nanoparticulate metal surface sites. The chemical composition of the particulate material is closely linked to the scavenging intensity of ^{230}Th and ^{231}Pa, expressed as distribution coefficients between solid and solution. A comparison of ^{230}Th and ^{231}Pa inventories with mantle-derived ^{3}He as well as a mass balance of ^{230}Th and ^{231}Pa suggests continuous scavenging removal over the course of the entire 4000 km transect. Unlike the two radiogenic isotopes, ^{232}Th is enriched above what would be expected from assuming identical scavenging behavior to ^{230}Th, indicating a hydrothermal source of colloidal, unreactive ^{232}Th.

1. Introduction

Throughout the global mid-ocean ridge system, hydrothermal circulation occurs when cold seawater percolates through and reacts with the upper ocean crust, heating to temperatures surpassing 400 °C. After reacting with the host rock, the hot, geochemically-altered fluids are sufficiently buoyant to rise back towards the ocean floor, where they are re-emitted into the deep ocean via submarine vents. The fluid rapidly mixes with ambient seawater and rises to form a neutrally buoyant hydrothermal plume (German and Seyfried, 2014). Due to high particle abundance (e.g. Estapa et al., 2015; Feely et al., 1987) and unique chemical and isotopic composition with respect to ambient deep ocean waters (German and Seyfried, 2014), hydrothermal activity has great potential for modulating elemental budgets and ocean chemistry.

Studies have identified hydrothermal plumes as a large source of many elements, such as iron and manganese (Klinkhammer et al., 1977; Resing et al., 2015; Saito et al., 2013), zinc (Von Damm et al., 1985; Roshan et al., 2016), and a large sink for many others, including rare earth elements (German et al., 1990), uranium (Michard and Albarède, 1985), and thorium (German et al., 2002; German et al., 1991; Kadko, 1996), via adsorption onto or co-precipitation with hydrothermal particles.

Whether hydrothermal plumes exert basin-scale influence on geochemical budgets in the ocean has been a much-debated topic. Hydrothermal inputs of iron have received significant attention (Tagliabue et al., 2014, 2010; Tagliabue and Resing, 2016) due to the biological necessity of Fe and the broad regions of the surface ocean in which primary production is limited by a lack of iron (e.g. Falkowski
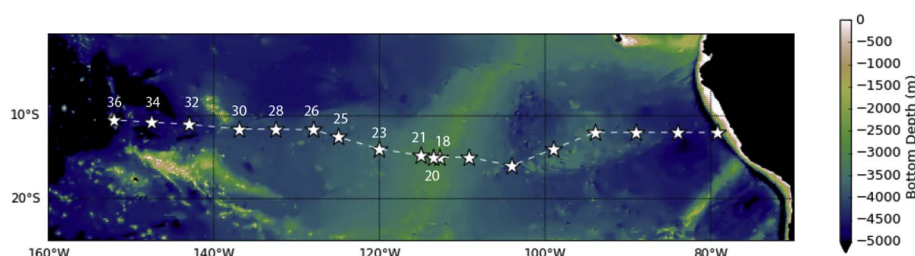
Fig. 1. Locations of the GP16 full-depth stations overlying seafloor bathymetry. Stations for which results are presented here are numbered.

et al., 1998). Early studies argued that, despite iron being heavily enriched (10^6 times greater than seawater) in hydrothermal vent fluids, the long-range effect of hydrothermal activity on dissolved iron content in the deep ocean would be limited by rapid precipitation of oxides and sulfides when vent fluids initially come into contact with oxygenated seawater (Feely et al., 1996; German et al., 1991; Rudnicki and Elderfield, 1993). However, in recent years the paradigm of negligible far-field transport of hydrothermal iron has been upended by several studies finding plumes of dissolved iron and manganese thousands of kilometers away from their sources along the global mid-ocean ridge system, indicating that stabilization and/or slow oxidation rates in hydrothermal environments allow Fe to spread throughout entire ocean basins (Bennett et al., 2008; Fitzsimmons et al., 2014; Resing et al., 2015; Saito et al., 2013; Sander and Koschinsky, 2011). The long-range spread of plume particles and their influence on trace metal scavenging remain mysteries.

Two unique tracers of particulate scavenging are the long-lived radionuclides of protactinium (^{231}Pa) and thorium (^{230}Th), as their disequilibrium from production by parent nuclides (^{235}U and ^{234}U, respectively) provides a rare 'clock' for calculating removal rates with respect to adsorption onto particles. Dissolved uranium is conservative in the ocean and the distribution of uranium isotopes is well-mixed (Andersen et al., 2010), so the production rates of ^{231}Pa and ^{230}Th are well-known, and nearly constant throughout the ocean. Scavenging residence times for ^{231}Pa (50–200 years) and ^{230}Th (10–40 years) (Henderson and Anderson, 2003) are much shorter than their respective half-lives of 32,760 years (Robert et al., 1969) and 75,584 years (Cheng et al., 2013) so their removal from the water column can be treated as being quantitatively equal to their known production rates. Water column variations in the activities of ^{231}Pa and ^{230}Th are the result of factors related to their removal, redistribution, or partitioning between phases – factors such as particle flux, particle composition, advection, and diffusion.

Much like iron, early studies on the scavenging of ^{230}Th and ^{231}Pa in hydrothermal plumes were focused on sites nearby ridge crest sources. Ridge flank sediments showed enhanced removal of ^{230}Th and ^{231}Pa associated with downcore peaks in Fe and Mn content, reflecting hydrothermal scavenging (German et al., 1997, 1993; Shimmield and Price, 1988). However, peaks in ^{230}Th and ^{231}Pa activity were not always associated with hydrothermal metal anomalies in these cores.

Other studies focused on the signature of hydrothermal scavenging in the water column. German et al. (1991) found a positive, linear correlation between total (dissolved plus particulate) ^{230}Th and particulate Fe in samples within two kilometers of an active vent site at the TAG hydrothermal vent field. This is slightly unexpected, given that high concentrations of sinking particles would be expected to generate a deficit of ^{230}Th. The authors argued that the elevated total ^{230}Th was the result of re-entrainment of particles that had previously sunken out of the hydrothermal plume.

German et al. (2002) measured particulate ^{230}Th in sediment trap samples from within 20 m of an active hydrothermal vent site at 13°N on the East Pacific Rise, and found ^{230}Th fluxes three times greater than in the overlying water column. This was explained by adsorption of dissolved ^{230}Th onto particles setting up a strong dissolved ^{230}Th gradient away from vent activity, with the resulting diffusive transport

causing ^{230}Th on sinking particles to be greater than what was produced in overlying waters. The spatial extent of this lateral diffusive input flux is not well understood. Only recently have mid-depth ^{230}Th deficits at sites thousands of kilometers away from ridge systems been attributed to hydrothermal scavenging. Lopez et al. (2015) found a depletion in dissolved and total ^{230}Th in ~2500 m depth waters in the Central Equatorial Pacific, 5000 km downstream of the East Pacific Rise (EPR). These authors attributed their signal to depletion of ^{230}Th from the water column by near-axis hydrothermal scavenging, and subsequent advection of the depletion signal westward towards their site.

Here we present dissolved and particulate ^{230}Th, ^{231}Pa, and ^{232}Th data from a hydrothermal plume in the South Pacific Ocean extending over 4000 km away from the EPR. We use the radioactive disequilibrium of these nuclides in the dissolved phase and enrichment in the particulate phase to understand the particle dynamics and scavenging behavior of trace metals in regions of intense hydrothermal activity.

2. Materials and methods

2.1. Cruise setting and sample collection

GEOTRACES cruise GP16 took place between Manta, Ecuador and Papeete, Tahiti aboard the RV Thomas G. Thompson between 25 October and 20 December 2013 (Fig. 1). Sampling for dissolved and particulate protactinium and thorium isotopes took place at 20 stations, 10 of which are downstream of the South East Pacific Rise (SEPR) ridge axis, and one of which (Station 18) lies directly above the ridge axis. The SEPR is one of the fastest-spreading ridge systems in the world, with a spreading rate of roughly 14.5 cm yr^{-1} (Feely et al., 1996). Hydrothermal activity along the SEPR is well-documented by anomalously high mantle-derived ^{3}He (^{3}He$_{xs}$) downstream of the ridge axis throughout the Pacific Basin (Lupton and Craig, 1981), as well as the areal extent of metalliferous sediments surrounding the ridge system (Boström et al., 1969). Along 11–15°S, independent lines of evidence point towards topographically-steered westward flow between 2000 and 3000 m depth above the ridge axis (Faure and Speer, 2012; Hautala and Riser, 1993; Reid, 1986), placing the GP16 stations west of the SEPR downstream of the hydrothermal activity along the ridge axis.

2.2. Sample collection and analysis

Radionuclide samples were collected according to standard GEOTRACES protocols (Anderson et al., 2012), then analyzed by two intercalibrated labs: Lamont-Doherty Earth Observatory of Columbia University (LDEO) and University of Minnesota (UMN). For dissolved samples, 4–5 l of seawater were filtered through a 0.45 μm Acropak capsule filter at sea and acidified to pH = 2 using 6 M hydrochloric acid. Particulate samples were collected with McLane Research Laboratories in-situ pumps, using a 51 μm polyester screen to collect particles > 51 μm, followed by two stacked 0.8 μm filters to collect small particles (0.8–51 μm). Details of the sampling methodology for collecting particulate samples for radionuclide analysis can be found in Hayes et al. (2015a). The full procedure describing analysis of particulate samples for composition can be found in Lam et al. (this issue).
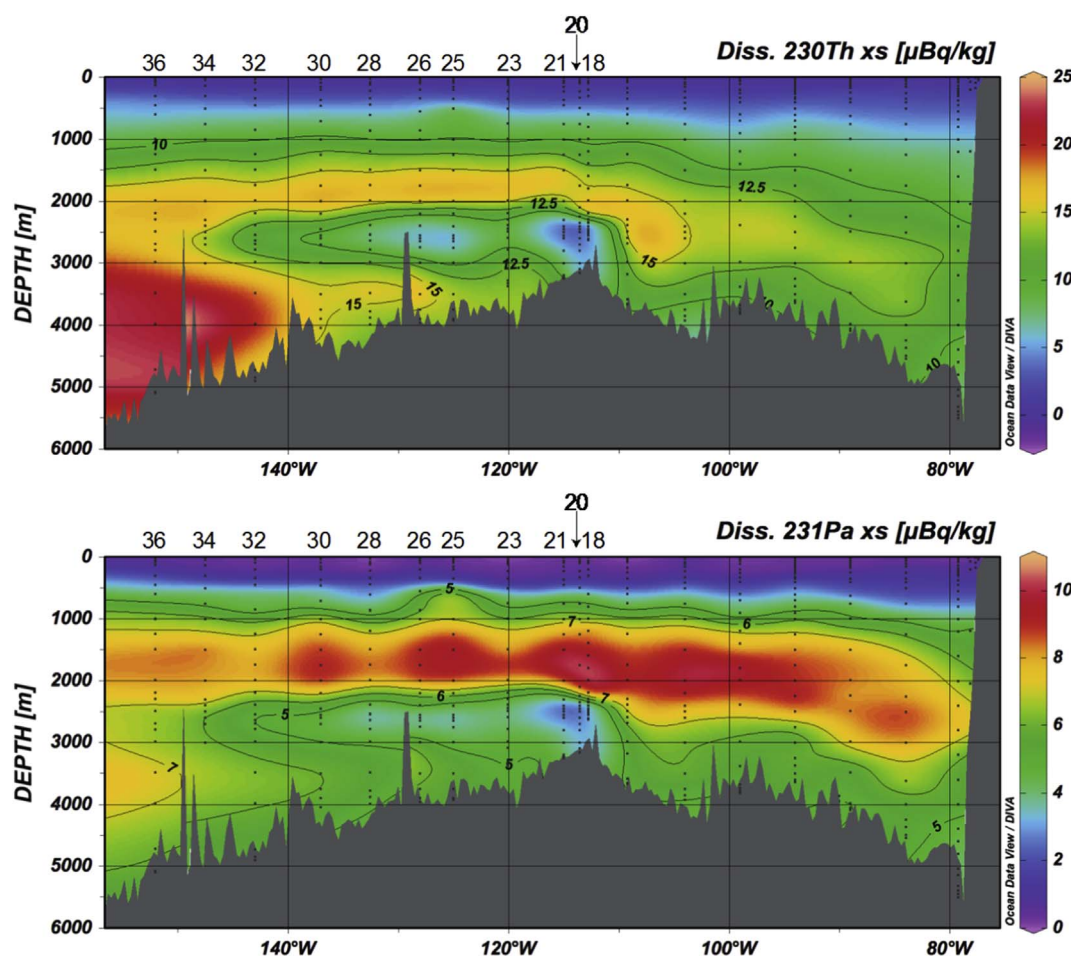
Fig. 2. Sections of dissolved $^{230}Th_{xs}$ and $^{231}Pa_{xs}$ activities on GP16. Station numbers for which results are presented here are indicated across the top of each station.

Briefly, biogenic opal was determined by spectrophotometry, particulate organic carbon in the small size fraction was determined by flash combustion, and particulate inorganic carbon was measured by coulometry. The mass of lithogenic materials was determined by measuring aluminum via digestion and subsequent analysis by inductively-coupled plasma mass spectrometry (ICP-MS). Particulate aluminum concentrations were then divided by the Al content of upper continental crust (UCC) to determine the mass of particulate lithogenic material. Particulate concentrations of Fe oxyhydroxides and Mn oxides were determined as excess Fe and Mn over their lithogenic contributions, by subtracting lithogenic Fe and Mn from bulk Fe and Mn concentrations (measured by ICP-MS) using Al concentrations and Fe/Al and Mn/Al ratios in UCC, and assumed to have the compositions $Fe(OH)_3$ and MnO_2. Total suspended particulate mass (SPM) was determined by summing the individual particulate components: Particulate organic matter, opal, calcium carbonate, lithogenics, Fe oxyhydroxides, and Mn oxides.

The analysis procedures for ^{230}Th and ^{231}Pa are as follows. All samples were stored and analyzed on-shore. Dissolved samples were spiked with ^{229}Th and ^{233}Pa, co-precipitated with Fe oxyhydroxide, pre-concentrated, and digested with HNO_3, HF, and $HClO_4$. Filter samples were completely dissolved using HNO_3 and $HClO_4$ before iron co-precipitation (Hayes et al., 2015a). Both dissolved and particulate thorium and protactinium isotopes were then isolated using anion exchange chromatography and analyzed using ICP-MS. Full details of the LDEO and UMN analytical procedures are documented in Anderson et al. (2012) and Shen et al. (2002, 2012, 2003). Dissolved samples are corrected for ingrowth of ^{230}Th and ^{231}Pa by uranium decay during sample storage. We then apply two separate corrections. When

evaluating the effects of scavenging on radionuclides in the water column, we correct both dissolved and particulate ^{230}Th and ^{231}Pa for lithogenic contributions, as outlined by Hayes et al. (2013b). Data corrected in this manner typically have the subscript xs. With the exception of calculating distribution coefficients (K_d), all measurements and discussions of ^{230}Th and ^{231}Pa are corrected for ingrowth during sample storage and lithogenic contributions. However, when calculating distribution coefficients, we assume that the dissolved Th and Pa from dissolution of lithogenic materials will be equally likely to participate in adsorption and desorption reactions as the dissolved Th and Pa from uranium decay in the water column. Following Hayes et al. (2015b), the particulate pool of ^{230}Th and ^{231}Pa used for determining K_d values is the sum of the xs particulate concentration and the adsorbed component of the lithogenic contribution. We denote $^{230}Th_p^{ads}$ as the combination of these two pools. GEOTRACES GP16 data are archived at the Biological and Chemical Oceanography Data Management Office (BCO-DMO), both for radionuclides (http://www.bco-dmo.org/dataset/643639) and particulate composition (http://www.bco-dmo.org/dataset/668083). These datasets will also be included in the 2017 GEOTRACES Intermediate Data Product.

2.3. Blanks and uncertainties

Procedural blanks for dissolved samples were determined by processing 5 l of Milli-Q water in acid-cleaned cubitainers, acidified to pH = 2 using 6 M HCl. Average procedural blanks for dissolved samples were 7 pg ^{232}Th, 0.4 fg ^{230}Th, and 0.1 fg ^{231}Pa. For particulate samples, blanks were measured using "dipped blanks" – acid-cleaned filters deployed on each pump cast, but with no seawater pumped over

them (Lam et al., this issue). The pooled average of all dipped blanks were used for background correction, and were 21.52 pg ^{232}Th, 1.17 fg ^{230}Th, and 0.07 fg ^{231}Pa.

For thorium, measurement uncertainties include propagated errors from ICP-MS isotope ratio measurements, spike concentrations, and blank corrections. For protactinium, uncertainties included the same factors as for thorium, but also instrumental mass bias, yield correction, and machine blank. In addition to analytical precision, we also assessed the long-term reproducibility of our measurements by measuring aliquots of two standard solutions containing ^{232}Th, ^{230}Th, and ^{231}Pa: SW STD 2010-1 (Anderson et al., 2012) and SW STD 2015-1. Standard measurements during analysis of dissolved samples gave reproducibility of 1.44% for ^{230}Th, 2.14% for ^{232}Th, and 3.89% for ^{231}Pa. During analysis of particulate samples, reproducibility was 1.03% for ^{230}Th, 1.12% for ^{232}Th, and 2.95% for ^{231}Pa.

3. Results and discussion

3.1. Hydrothermal scavenging of ^{230}Th and ^{231}Pa

In this paper, we primarily focus on data from below 1000 m depth from the stations west of the EPR along GP16. The multitude of other features affecting ^{230}Th and ^{231}Pa along the eastern portion of the section and in the upper 1000 m will be the subjects of future work. In the upper 2000 m, dissolved and particulate ^{230}Th and ^{231}Pa display the linear increase with depth predicted by reversible scavenging (Bacon and Anderson, 1982). At stations west of the EPR, strong depletions in ^{230}Th and ^{231}Pa are present below 2000 m (Fig. 2), coincident with the depths of hydrothermal enrichment of dissolved ^{3}He$_{xs}$ (Jenkins et al., this issue), Fe, Mn, Al, (Resing et al., 2015) and Zn (Roshan et al., 2016) along the same section. The depth of the minima in dissolved ^{230}Th and ^{231}Pa varies by < 100 m across the section, between 2500 and 2600 m,

below which ^{230}Th and ^{231}Pa increase towards the bottom (Fig. 3). Conversely, particulate ^{230}Th and ^{231}Pa are enriched below 2000 m, with maxima at similar depths as the dissolved minima, before decreasing towards the seafloor (Fig. 3). This hydrothermal scavenging signal persists at all sampling locations west of the ridge axis (stations 18–36), over 4000 km away from the vent sites along the EPR (Fig. 2).

Reversible scavenging predicts that 1-dimensional profiles of dissolved, particulate, and total ^{230}Th and ^{231}Pa will increase linearly with depth (Bacon and Anderson, 1982). Deviations from reversible scavenging at depth must therefore reflect some combination of local anomalous scavenging behavior and lateral dispersal (Hayes et al., 2015a). The reversible scavenging model provides a baseline against which hydrothermal scavenging can be quantified. As previously suggested (Deng et al., 2014; Hayes et al., 2015a) and performed (Lopez et al., 2015), we quantify the degree of hydrothermal scavenging as a percent depletion of total ^{230}Th and ^{231}Pa relative to the expected concentration at depth due to reversible scavenging (Fig. 4a).

We first predict reversible scavenging profiles of total ^{230}Th and ^{231}Pa based on a regression of concentration and depth between 300 and 1500 m. The depth ranges were chosen to avoid changes in slope present in the uppermost water column (Hayes et al., 2015c) and hydrothermal influence at depth. We extrapolate the derived regressions to depths below 1500 m to calculate the values of total ^{230}Th and ^{231}Pa concentration predicted by reversible scavenging if no hydrothermal plume were present. Concentrations in this 300–1500 m depth range are nearly the same everywhere (Fig. 3) so we compute only one reversible scavenging prediction each for ^{230}Th and ^{231}Pa. The observed concentration-depth relationships have correlation coefficients of $R^2 = 0.98$ for ^{230}Th, and $R^2 = 0.96$ for ^{231}Pa. Following Resing et al. (2015), we designate the depth range of the hydrothermal plume as being between 2200 and 2800 m. For stations at which those exact depths were not sampled, we linearly interpolate ^{230}Th and ^{231}Pa onto
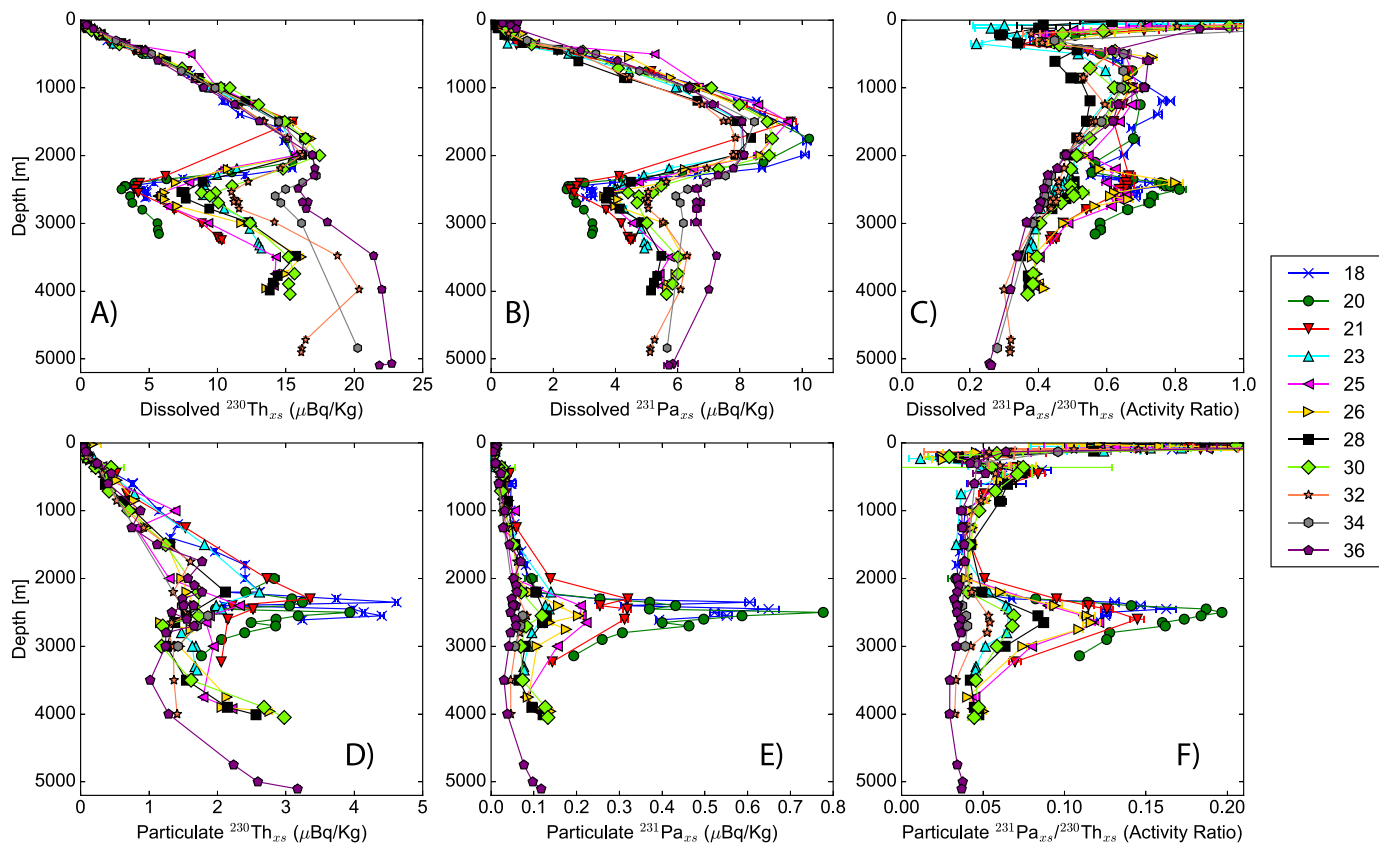

Fig. 3. Profiles of A) Dissolved ^{230}Th$_{xs}$, B) Dissolved ^{231}Pa$_{xs}$, C) Dissolved xs ^{231}Pa/^{230}Th activity ratio, D) Particulate ^{230}Th$_{xs}$, E) Particulate ^{231}Pa$_{xs}$, F) Particulate xs ^{231}Pa/^{230}Th activity ratio. Error bars represent 1-sigma measurement uncertainty. Where not visible, error bars are smaller than the symbol size.
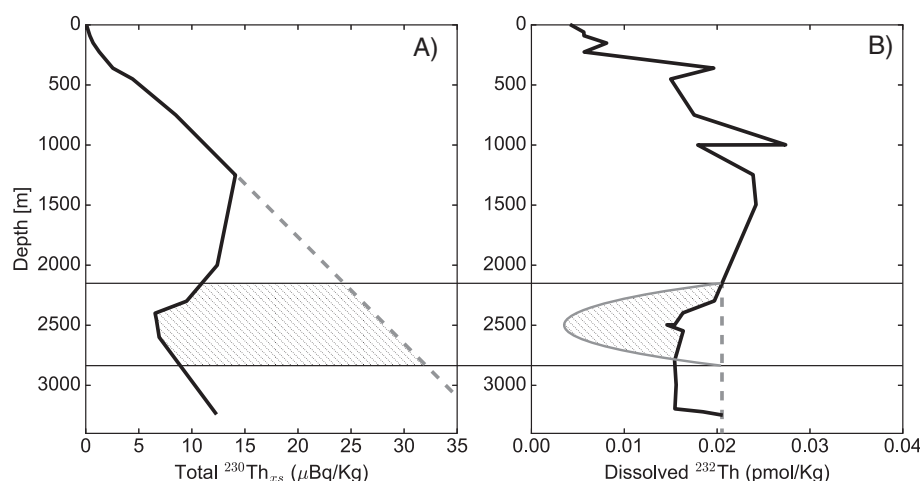
Fig. 4. Schematics explaining calculations used in text. Horizontal lines outline the 2200–2800 m depth range used to define the hydrothermal plume. Thick black lines are observed profiles from Station 21. Dashed lines indicate profiles expected from the reversible scavenging model. A) Depletion of ^{230}Th (also used for ^{231}Pa) shown in hatched area between the observed profile and the profile expected if only reversible scavenging were occurring. B) Extra ^{232}Th$_{add}$ from hydrothermal input. Hatched area is the difference between the observed profile (heavy solid line) and the ^{232}Th expected (solid gray line) from applying the percent depletion of dissolved ^{230}Th to ^{232}Th. Hatched area represents an inventory of ^{232}Th that cannot be accounted for by supply from above the plume by reversible scavenging, which we attribute to a source of colloidal ^{232}Th delivered by hydrothermal activity.

those depths to facilitate integration within that range. Given the activity predicted by extrapolation of upper water column profiles ($A_{predicted}$) and the measured activity ($A_{measured}$) of total ^{230}Th or ^{231}Pa at each depth, we calculate percent depletion:

$$\text{Percent Depletion} = \frac{\int_{2200}^{2800} A_{predicted}(z) - A_{observed}(z)^*}{\int_{2200}^{2800} A_{predicted}(z)} 100 \qquad (1)$$

While the terms in the equation are the same as in Lopez et al. (2015), note that we only integrate within the depth range of the hydrothermal plume, whereas Lopez et al. integrate over the full water column. We choose the narrower range to avoid potential influences of bottom water advection and nepheloid layer scavenging on our calculation. Consequently, it is possible that we underestimate the hydrothermal scavenging at some stations, especially those nearest to the ridge axis, where the scavenging signal might extend beyond the depth range of our integration window.

Removal of ^{230}Th and ^{231}Pa is greatest at the ridge axis, both peaking near 70% depletion, before decreasing as waters move west away from the EPR (Figs. 3a, b, and 5). By station 36, ^{230}Th only has 30% depletion, while ^{231}Pa maintains 55% depletion. To assess how geographically widespread the hydrothermal scavenging signature in ^{230}Th and ^{231}Pa might be, we compare percent depletion to the age of the plume waters since they left the EPR ridge axis – referred to as the plume age. Resing et al. (2015) found that station 18 had a low ^{3}He$_{xs}$ inventory compared to stations further west of the ridge axis, suggesting that the far-field hydrothermal plume is supplied by vents further south on the EPR, whereas station 18 is not. As a result, we use

station 20, rather than station 18, as the initial point for deriving plume ages. For each station, we divide the distance to station 20 by a westward advection velocity of 0.4 cm/s (Hautala and Riser, 1993) to determine the plume age. We perform a linear regression of percent depletion and plume age, with $R^2 = 0.79$ for ^{230}Th and $R^2 = 0.89$ for ^{231}Pa. By extrapolating the regressions to 0% depletion, we can determine the amount of time a hydrothermal scavenging signal will persist in the ocean for Th and Pa. We calculate depletion timescales (age of zero depletion) of 64 years for ^{230}Th, and 140 years for ^{231}Pa. The depletion timescale of ^{230}Th is long enough to validate the far-field findings of ^{230}Th depletion seen along the Equator and near 8°N by Lopez et al. (2015), as well as their supposition about hydrothermal scavenging being responsible for the mid-depth ^{230}Th depletion seen in the Eastern Tropical North Pacific by Okubo et al. (2012). The zonal flows in the abyssal Pacific (e.g. Johnson and Talley, 1997; Stommel, 1982) allow for the persistence of the scavenging signal throughout the Pacific basin, whereas in the North Atlantic, along-segment flow (Thurnherr et al., 2002) may largely prevent the scavenging signal to be widespread beyond the confines of the axial valley of the Mid-Atlantic Ridge (MAR), although on the US GEOTRACES GA03 transect a small scavenging signal is also seen in the first station to the west of the MAR as well (Hayes et al., 2015a).

3.2. What process or phase is scavenging ^{230}Th and ^{231}Pa?

3.2.1. Distribution coefficients and fractionation factors

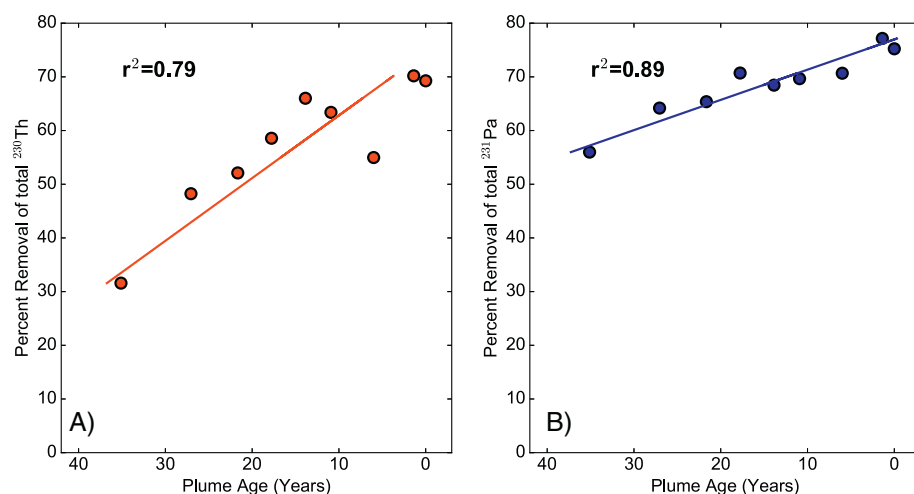The greater residence time of ^{231}Pa compared to ^{230}Th in the open

Fig. 5. Percent depletion of A) total ^{230}Th$_{xs}$ and B) total ^{231}Pa$_{xs}$ plotted against the plume age, with Station 20 set at 0 age, using the distance of each station from station 20 divided by a constant plume spreading rate of 0.4 cm/s to estimate age. Points are derived for the 2200–2800 m depth interval at each station using Eq. (1). Lines are linear regressions of percent removal with plume age.

ocean is explained by the lower reactivity with respect to adsorption onto particles of ^{231}Pa (Anderson et al., 1983a). However, the two nuclides display different affinity for different particle types (Anderson et al., 1983b; Chase et al., 2002; Geibert and Usbeck, 2004; Hayes et al., 2015b; Kretschmer et al., 2011). As a result, the relative removal rates of ^{231}Pa and ^{230}Th can vary with particle composition. Greater particle abundance will also affect the scavenging intensity of both ^{231}Pa and ^{230}Th. To determine the relative roles of particle composition and particle abundance on the scavenging of ^{231}Pa and ^{230}Th, we calculate the bulk partition coefficient (K_d) values, defined in units of activity per gram of particles divided by activity per gram of seawater:

$$K_d = \frac{A_{ads}^p}{A^{diss}} \times \frac{1}{SPM} \qquad (2)$$

The units of A_{ads}^p and A^{diss} are both activities per kg of seawater, while SPM has units of grams of particles per gram of seawater. In addition, we calculate the fractionation factor (Anderson et al., 1983a) defining the relative scavenging intensity of ^{230}Th to ^{231}Pa:

$$F\left(\frac{Th}{Pa}\right) = \frac{K_d^{Th}}{K_d^{Pa}} \qquad (3)$$

Particle concentration is thought to play an important role in modulating the scavenging intensity (K_d) of thorium and protactinium. K_d values for ^{234}Th (Honeyman et al., 1988), compilations of both ^{234}Th and ^{230}Th (Hayes et al., 2015b; Henderson et al., 1999), and ^{231}Pa (Hayes et al., 2015b) have reciprocal relationships with particle mass, known as the "particle concentration effect". Why K_d values decrease with increasing particle mass is not entirely understood. One possibility is that higher concentrations of thorium-binding colloids small enough to pass through typical filters keep the apparent ^{230}Th concentration artificially high in the dissolved phase (Henderson et al., 1999). Another suggestion is that surface area per mass of particle decreases at greater particle mass, thereby reducing the number of available binding sites for scavenging metals (Henderson et al., 1999). Finally, recent inverse model estimates of thorium scavenging kinetics from the GA03 North Atlantic Zonal Transect cruise suggest that the rate at which thorium desorbs from particles appears to be positively correlated with particle concentration, which would also give rise to an apparent particle concentration effect (Lerner et al., 2017).

We compare the relationship between K_d values for Th and Pa and SPM for the entire GP16 section with the relationship derived using exclusively the samples influenced by the hydrothermal plume, stations 18–30, from 2200 to 2800 m depth (Fig. 6). Linear regressions for the non-plume samples of Log K_d with Log SPM from the small size fraction (SSF) have the trends Log K_d(Th) [g/g] = 8.04–0.874*Log SPM [µg/l] (R^2 = 0.72, p < 0.001); Log K_d(Pa) [g/g] = 6.79–0.48*Log SPM [µg/l] (R^2 = 0.28, p < 0.001). The samples from the plume form an array above the rest of the samples from the transect, indicating that whatever processes generate that negative correlation between K_d and SPM

are not responsible for the K_d variations observed in the hydrothermal plume. In addition, the narrow range of SPM concentrations observed in the plume is too small for there to be a major particle concentration effect on K_d values. The particle concentration effect only becomes apparent when K_d is evaluated over particle concentrations spanning at least an order of magnitude.

The observed correlation between K_d and SPM can be used to show the driving force behind the hydrothermal scavenging of ^{230}Th and ^{231}Pa. We define K as the ratio of particulate adsorbed to dissolved ^{230}Th or ^{231}Pa. From Eq. (2), it is apparent that K can be calculated by multiplying K_d with SPM. By calculating expected K_d values for all samples using the statistical relationship between log K_d and log SPM, along with the measured SPM concentration, we can then calculate an expected K value for samples within the hydrothermal plume using the equation:

$$K^{exp} = K_d^{exp} * SPM^{meas} \qquad (4)$$

Here, K^{exp} is the expected K value, K_d^{exp} is the expected K_d value calculated from the observed SPM concentration and the Log K_d-SPM regressions for Th and Pa, SPM^{meas} is the measured SPM (Lam et al., this issue). The observed K values for both Th and Pa exceed the K values expected from the SPM concentration in the hydrothermal plume (Fig. 7). These higher than expected K values and hydrothermal samples falling well above the K_d-SPM relationships (Fig. 6) show that high particle concentration cannot be the primary mechanism responsible for the observed hydrothermal scavenging of ^{230}Th and ^{231}Pa on GP16.

The scavenging intensity of ^{230}Th and ^{231}Pa is also dictated in part by the composition of particles present in the water column. Early studies on the controls of scavenging intensity hypothesized that metal (particularly manganese) oxides play a critical role in the adsorption of dissolved trace metals onto particle surfaces (Anderson et al., 1983b; Balistreri and Murray, 1986). Since then, it has been shown that despite making up a small fraction of the total suspended material throughout most of the ocean, Mn and Fe (oxyhydr-)oxide particles play an outsized role in scavenging ^{230}Th and ^{231}Pa. Both experimental (Geibert and Usbeck, 2004) and observational (Anderson et al., 1983b; Hayes et al., 2015b; Roy-Barman et al., 2009) studies have found that the K_d of MnO_2 is at least an order of magnitude greater than that of other constituents (e.g. $CaCO_3$ and lithogenics) for both protactinium and thorium. Performing a nonlinear least squares regression to solve for endmember K_d values of six particle constituents (POM, $CaCO_3$, lithogenics, opal, $Fe(OH)_3$, and MnO_2), Hayes et al. (2015b) found that the K_d of iron oxyhydroxides was an order of magnitude greater than that of POM, $CaCO_3$, and lithogenics, and that the K_d of manganese oxides was an order of magnitude greater than that of iron oxyhydroxides.

Hydrothermal vent fluids are highly enriched in Fe and Mn (Von Damm et al., 1985; Klinkhammer et al., 1977). When these reducing vent fluids are released into high-O_2 seawater, the dissolved Fe (that
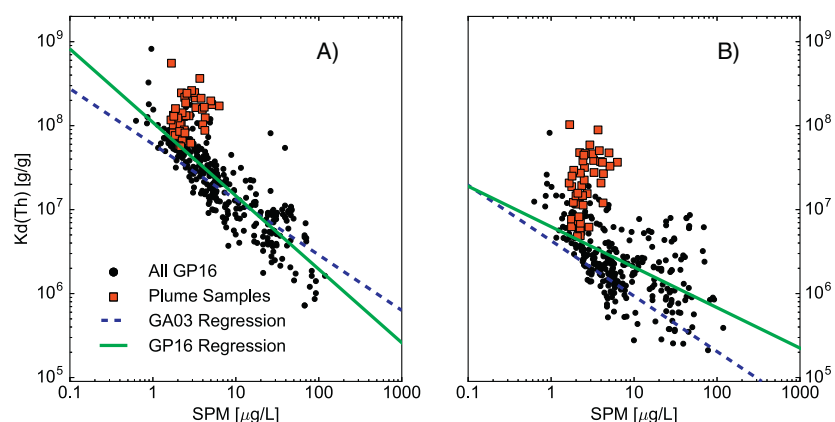

Fig. 6. Crossplots showing relationships between K_d values of ^{230}Th (A) and ^{231}Pa (B) with SPM concentration. Both x- and y-axes are plotted on log-scales. In black are all non-hydrothermal plume samples from GP16. In red are samples from the hydrothermal plume – from Stations 18–30, between 2200 and 2800 m depth. Blue lines show the best-fit linear regression between log K_d and log SPM from the GA03 (Hayes et al., 2015b) section in the North Atlantic. Green lines show the best-fit linear regression between log K_d and SPM for non-hydrothermal samples from the GP16 section. (For interpretation of the references to colour in this figure legend, the reader is referred to the web version of this article.)
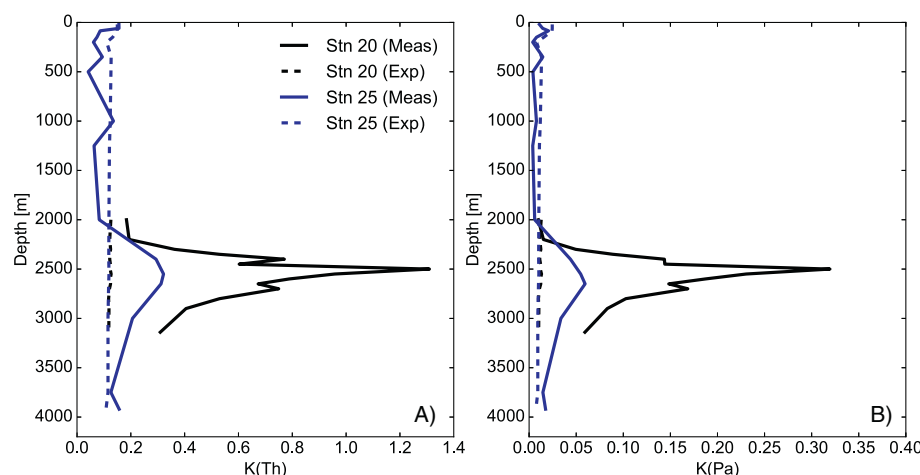
Fig. 7. Measured and expected K values (particulate activity/dissolved activity) for A) ^{230}Th and B) ^{231}Pa at two stations from GP16. Expected K values determined by calculating expected K_d values from the observed K_d-SPM relationships (Fig. 6), and multiplying the expected K_d values by the measured SPM concentration Eq. (4).

does not precipitate out as sulfides) and Mn oxidize (Mottl and McConachy, 1990) to form particles with high capacity for scavenging trace elements from seawater (German et al., 1990; Kadko et al., 1994). We investigate the role of iron and manganese oxides in scavenging ^{230}Th and ^{231}Pa using calculated distribution coefficients and fractionation factors along GP16, observed variations in particle mass, particulate iron oxyhydroxide and manganese oxide concentrations (Lam et al., this issue), together with the endmember K_d values and fractionation factors for iron and manganese oxides from Hayes et al. (2015b).

Near 1500 m depth on GP16, above the plume, bulk log(K_d) values range from 7.4–7.8 for thorium, and 6.2–6.5 for protactinium, with fractionation factors of 14–16 (Fig. 8). Within the depth range of the plume at stations closest to the EPR ridge axis (Stations 18–21), the log (K_d) increases to 8.2–8.8 for thorium and 7.4–8 for protactinium, while the fractionation factor decreases to 4–5.5 (Figs. 8 and 9). As the plume moves west beyond station 21, the K_d's of both thorium and protactinium decrease and the fractionation factor increases towards background levels by station 36 (Fig. 9). The maximum log(K_d) values observed for ^{230}Th nearly match the endmember K_d value of 8.5 for iron oxyhydroxides (Table 1). However, the log(K_d) values of ^{231}Pa at stations 18–21 are regularly around 7.7, with a maximum of nearly 8.0 (Fig. 8). Endmember log(K_d) values for ^{231}Pa of 7.46 for iron oxyhydroxides and 8.32 for manganese oxides imply that a much greater fraction of ^{231}Pa is scavenged by manganese oxides compared to ^{230}Th, which is primarily scavenged by Fe oxyhydroxides (Table 1). This is supported by the observed fractionation factors, which are at or just below 5, similar to the endmember fractionation factors for MnO_2 of 5.5 and POM of 4.9, and much lower than the $Fe(OH)_3$ endmember fractionation factor of 11.2 (Hayes et al., 2015b). We propose two hypotheses that could explain the observed K_d, F, and particle composition and concentration data. The first is that ^{230}Th and ^{231}Pa are scavenged by direct adsorption onto metal oxide surfaces. The second is that ligands binding dissolved ^{230}Th and ^{231}Pa are co-precipitated during Fe and Mn oxide formation, along with the radionuclides they chelate. We consider the evidence for and potential implications of these two hypotheses below.

3.2.2. Direct scavenging by metal oxide particles

The similarity of the K_d values of ^{230}Th and ^{231}Pa for a mixture of iron oxyhydroxide and manganese oxides, described above, supports direct adsorption to metal oxide surfaces. This hypothesis is also supported by comparison to K_d values and particle composition observed at the TAG hydrothermal vent site sampled on the GEOTRACES GA03 section (Station GT11-16) in the North Atlantic. At TAG, dissolved (Hatta et al., 2015) and particulate (Lam et al., 2015) Mn/Fe ratios are both lower than at Stations 18 and 20 on GP16. There was no evidence for MnO_2 precipitation at TAG, but there were direct measurements of

abundant iron oxyhydroxides (Lam et al., 2015). The lack of MnO_2 precipitation at TAG was previously observed by Trocine and Trefry (1988), and likely reflects the slow oxidation kinetics of Mn and the young age (~2 days) of the TAG plume (Kipp et al., this issue). The log K_d values for ^{230}Th and ^{231}Pa at TAG reach maxima of 8.26 and 7.15, respectively, while the minimum observed fractionation factor is 9.59 (Hayes et al., 2015b). The TAG K_d values are lower and the fractionation factor higher than observed at Stations 18 and 20 on GP16. The fractionation factor is much closer to the $Fe(OH)_3$ endmember, indicating that iron is the primary scavenger at TAG, with manganese playing a diminished role due to the lack of Mn particles. At GP16, the higher particulate Mn/Fe ratio results in a greater relative contribution of Mn particles to scavenging of trace metals in the hydrothermal plume, and less fractionation of Th from Pa in comparison to TAG. Additionally, on GP16, Station 18 has more particulate $Fe(OH)_3$ relative to station 20, but less MnO_2 relative to station 20 (Fig. 8). The particulate ^{231}Pa/^{230}Th activity ratio (Fig. 3) increases coincident with the increase in MnO_2 from station 18 to 20 (Fig. 8), reflecting the greater scavenging affinity of Mn for ^{231}Pa relative to other particulate phases. The K_d values of both ^{230}Th and ^{231}Pa also increase from Station 18 to 20 (Fig. 8), moving towards the higher K_d endmember of MnO_2. Together, these findings constitute strong evidence for direct adsorption to metal oxide surfaces, though not unequivocal.

There remain features that are difficult to explain if metal oxides are directly responsible for scavenging ^{230}Th and ^{231}Pa. SPM, $Fe(OH)_3$, and MnO_2 concentrations all decrease sharply between station 20 and station 21 (Fig. 8). Yet the K_d values of ^{230}Th and ^{231}Pa at station 21 are greater than those of station 18, and nearly as high as at station 20 (Fig. 8). Even at stations 25 and 26, far beyond where most of the metal oxides and SPM have been removed from the plume, K_d values remain anomalously high compared to background values (Fig. 9). At stations beyond 20, where SPM, $Fe(OH)_3$, and MnO_2 have all precipitously declined, how can the scavenging signature of metal oxides be maintained? We propose that even after most of the particle mass has been removed, the surface area of the particles remaining in the hydrothermal plume is predominantly metal surface coatings, predominantly Mn. The high K_d values at station 21, where the mass of particulate Fe $(OH)_3$ and Mn have sharply fallen (Fig. 8), requires that much of the high particulate $Fe(OH)_3$ and Mn mass at stations 18 and 20 must be bound within the inner matrix of particles, and, with no surface functional groups exposed to seawater, cannot bind solutes like ^{230}Th and ^{231}Pa. This is consistent with the size fractionation of Mn observed by Lee et al. (this issue), where 50% of the particulate Mn is predominantly in the > 51μm size fraction at stations 18 and 20, then decreases to 10–20% in the > 51 μm size fraction by station 21. Preliminary synchrotron X-ray microprobe results show that pMn in hydrothermal plume particles near the vent exist as a mixture of discrete Mn(IV)-
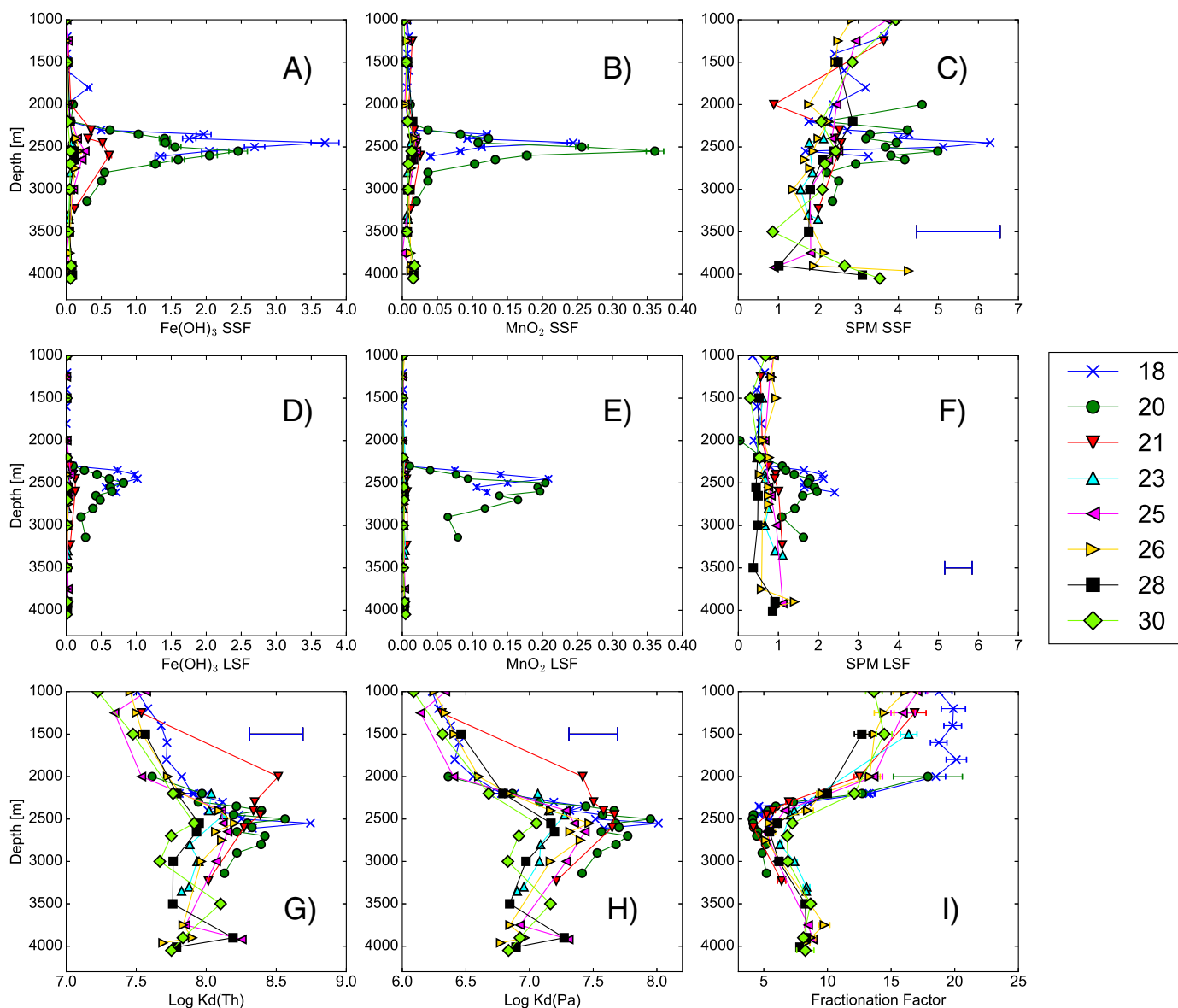
Fig. 8. Profiles, in μg/l, of Fe(OH)$_3$, MnO$_2$, and SPM in the 0.8–51 μm fraction (A–C), > 51 μm size fraction (D–F), and profiles of the logarithm of distribution coefficients for ^{230}Th (G), ^{231}Pa (H), and fractionation factor calculated for the 0.8–51 μm particle size fraction (I). Error bars indicate 1-sigma uncertainty. In A), B), D), E) and I), where error bars are not visible, uncertainties are smaller than the symbol size. In C), F), G), and H), a single error bar shows the average uncertainty for samples in the hydrothermal plume, between 2200 and 2800 m depth.
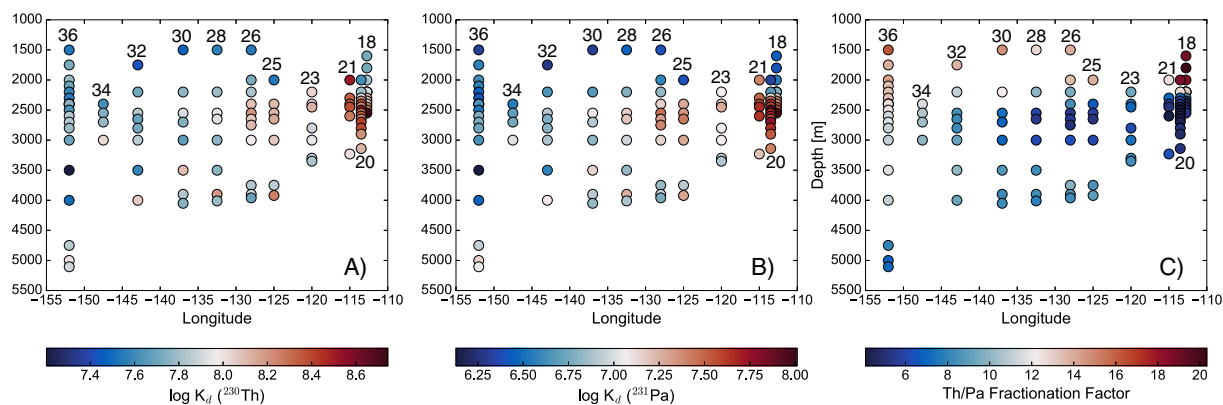
Fig. 9. Sections of A) log K$_d$(Th), B) log K$_d$(Pa) and C) Fractionation factor.

Table 1
Log K_d values for ^{230}Th and ^{231}Pa and fractionation factors (F) for individual particle phases (Hayes et al., 2015b), EPZT background deep waters not influenced by hydrothermal activity (station 17, 2600 m depth), EPZT hydrothermal plume (Station 18, 2550 m depth), and the TAG hydrothermal plume (Hayes et al., 2015b).

	logK$_d$(Th)	logK$_d$(Pa)	F(Th/Pa)
POM	6.48	5.30	4.9
Lithogenics	7.36	6.36	10
CaCO$_3$	7.48	5.95	33.3
Fe(OH)$_3$	8.52	7.47	11.2
MnO$_2$	9.07	8.33	5.5
EPZT background	7.78	6.62	14.41
EPZT plume	8.74	8.01	5.38
TAG plume	8.26	7.15	9.59

oxide particles and fine-coatings of an unidentified Mn-mineral (Lee and Lam, unpublished). We hypothesize that this latter form of nanoparticulate Mn coating could dominate the far-field particles. These combined effects would explain why there is little correlation between the mass of Fe(OH)$_3$ or MnO$_2$ with the K_d values for ^{230}Th and ^{231}Pa (Fig. 10). It also might help explain the decoupling of hydrothermal plumes and benthic nepheloid layers from the inverse relationship between SPM and K_d values for ^{230}Th and ^{231}Pa as observed in the Atlantic Ocean (Hayes et al., 2015b). Environments with high authigenic Mn precipitation will cause particles to have anomalously high fractions of their surface areas coated by nanoparticulate Mn relative to the mass of MnO$_2$ and the mass of particles present, causing the K_d values to be elevated.

Fractionation factors at 2500 m remain near 5 all the way to station 28, increasing towards background values by station 36 (Fig. 9). Even as K_d values have begun to fall by stations 25 and 26, low fractionation factors are maintained. The particulate MnO$_2$/Fe(OH)$_3$ ratio increases continuously from stations 25–34 (Fig. 10), which is difficult to reconcile with the conventional understanding of oxidation kinetics, wherein the oxidation of Fe(II) (e.g. Field and Sherrell, 2000) is much faster than the oxidation of Mn(II) (e.g. Cowen et al., 1990) in hydrothermal plumes. This may be related to the size partitioning and speciation of Mn and Fe in the GP16 hydrothermal plume. A significant fraction of operationally defined dissolved iron in hydrothermal plumes has been shown to exist as large colloids, rather than in a truly soluble phase (Fitzsimmons et al., 2014). In hydrothermal plumes, the dissolved-particulate partitioning of iron may be dictated by the kinetics of colloid aggregation-disaggregation (Fitzsimmons et al., 2017), while the dissolved-particulate partitioning of manganese may be more directly a function of oxidation kinetics, perhaps hastened by microbial activity (Cowen and Bruland, 1985; Cowen et al., 1986). On samples from the GP16 section, Fitzsimmons et al. (2017) found 63 ± 10% of dissolved Fe was colloidal, while only 2 ± 2% of dissolved Mn was colloidal. Colloid-bound Fe that aggregates into particles may not have the same surface area available for scavenging as nanoparticulate Mn mineral coatings on particles.

Slow, continuous precipitation of dissolved Mn controlling scavenging could cause fractionation factors close to that of MnO$_2$ to be maintained even in the distal plume, away from the highest pMn concentrations. This is supported by the depths of peak Fe, Mn, Th, and Pa concentrations. The depths of minimum dissolved and maximum
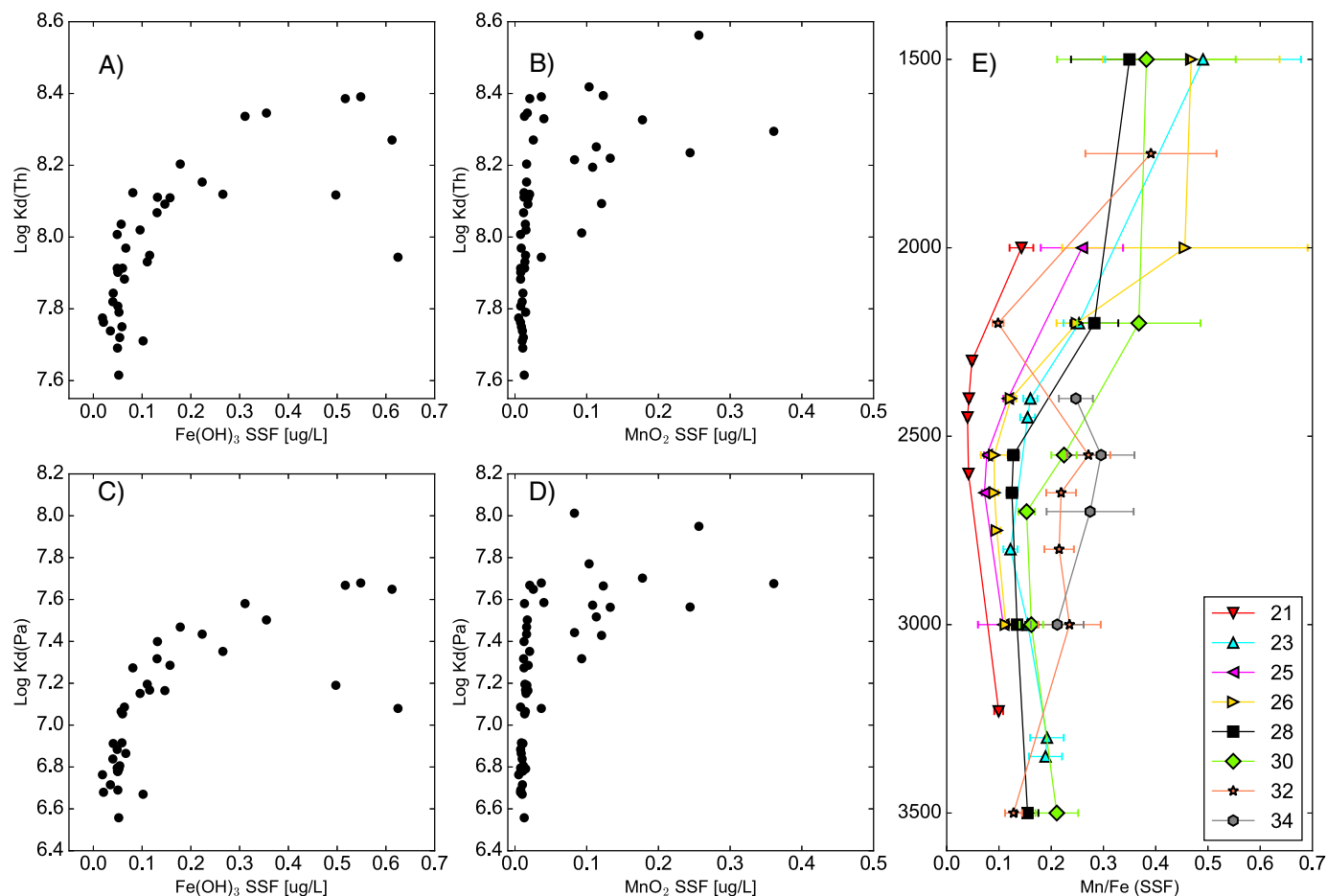

Fig. 10. Crossplots from the hydrothermal plume samples (Station 18–34, 2200–2800 m) of A) log Kd(Th) with particulate FeOH$_3$, B) log Kd(Th) with particulate MnO$_2$, C) log Kd(Pa) with particulate Fe(OH)$_3$, D) log Kd(Pa) with particulate MnO$_2$. E) The particulate Mn/Fe ratio above, within, and below the hydrothermal plume. Error bars in E) represent 1-sigma uncertainty. Where error bars are not visible, uncertainty is smaller than the symbol size.

particulate ^{230}Th and ^{231}Pa change very little over the course of the hydrothermal plume. Both pFe and dFe maxima are observed to sink nearly 350 m over the 4300 km length of the plume, however dMn and pMn peaks do not (Fitzsimmons et al., 2017). This supports a decoupling of ^{230}Th and ^{231}Pa scavenging from the colloidal aggregation-disaggregation kinetics governing Fe in the hydrothermal plume, and an association of ^{230}Th and ^{231}Pa scavenging with the precipitation of dMn into a non-sinking particulate phase.

However, hydrothermal maxima in both dissolved and particulate ^{231}Pa/^{230}Th activity ratios (Fig. 3) require a more rapid loss of thorium relative to protactinium in the near-field hydrothermal plume. If metal oxides are directly responsible for scavenging ^{230}Th and ^{231}Pa, one way this could be explained is by ^{230}Th being preferentially bound by Fe (OH)$_3$ particles and ^{231}Pa being preferentially scavenged by MnO$_2$ particles in the region closest to the ridge crest. Maxima in both the dissolved and particulate ^{231}Pa/^{230}Th activity ratios require more rapid removal of Th-binding Fe particles relative to Pa-binding Mn particles. Iron is thought to rapidly precipitate as sulfides and oxyhydroxides in the first days after eruption of hydrothermal plumes (Mottl and McConachy, 1990; Rudnicki and Elderfield, 1993; Trocine and Trefry, 1988), while manganese is less dynamic in this time interval (German and Seyfried, 2014). Given the high dissolved and particulate ^{231}Pa/^{230}Th activity ratios observed at station 18 (at the EPR), this would require preferential scavenging (adsorption and loss by sedimentation) of ^{230}Th in the buoyant plume – as the result of rapid precipitation of iron particles. This supports modeling efforts to explain the particulate Th/Fe ratios observed in neutrally buoyant plume samples (German et al., 1991) at TAG, which required rapid scavenging rates for thorium early in the history of the hydrothermal plume (Rudnicki and Elderfield, 1993).

3.2.3. Indirect scavenging by ligand co-precipitation

An abundance of evidence leads us to consider scavenging of ^{230}Th and ^{231}Pa to most likely be the result of direct adsorption to MnO$_2$ and Fe(OH)$_3$ surface functional groups for reasons described in the preceding sections. However, the results are not unequivocal, and could also be explained by the uptake and co-precipitation of ligands binding ^{230}Th and ^{231}Pa in solution. The low fractionation factors as far west as station 28 observed on GP16 (Fig. 9), are similar to the endmember F values of POM (Hayes et al., 2015b), but the inferred endmember K$_d$ values for both ^{230}Th and ^{231}Pa are orders of magnitude lower for POM (Log K$_d$ = 6.5 and 5.8, respectively) compared to Fe(OH)$_3$ and MnO$_2$ endmembers, and compared to the observed K$_d$ values in the hydrothermal plume on GP16 (Fig. 9). Ligands that bind thorium in solution are thought, at least to first order, to be similar to ligands which bind iron (Barbeau et al., 2001). On the GA03 section in the North Atlantic, iron-binding ligands were higher at the TAG hydrothermal vent site than in ambient deep ocean waters (Buck et al., 2015). Iron-binding ligands are often abundant in neutrally buoyant hydrothermal plumes (Bennett et al., 2008; Sander and Koschinsky, 2011), occasionally in excess of the labile iron concentrations (Kleint et al., 2016) and are hypothesized to be a major factor in stabilizing dissolved Fe as plumes advect far away from vent sites (Toner et al., 2009, 2012). On the GP16 section, biogeochemical ocean models were unable to reproduce the observed distribution of dissolved Fe west of the EPR without an equimolar hydrothermal input of ligands as well as iron (Resing et al., 2015).

The K$_d$ values for Th and Pa in the plume are orders of magnitude larger than for POM. For ^{230}Th and ^{231}Pa scavenging to be due to co-precipitation of ligands would therefore require the confluence of several factors. The observed K$_d$ values on GP16 would require that co-precipitation of ligands occurs by metal oxides stripping Th- and Pa-binding ligands out of solution with the metals still bound to them. This would have to happen while not subsequently affecting POM. The distribution coefficients of the Th- and Pa- binding ligands would have to have binding constants for Th and Pa that, when combined with the

adsorption constants to metal oxides of those ligands, result in observed fractionation factors within the plume that are similar to POM. While not impossible, it would require quite a few coincidences in the values of largely unconstrained variables for the observed fractionation factors to be due to ligand scavenging.

Fitzsimmons et al. (2017) argue that iron scavenging on GP16 reflects aggregation-disaggregation of iron-binding ligands. If iron binding ligands and thorium binding ligands are roughly similar in composition (Barbeau et al., 2001), then the observed evolution of particulate ^{230}Th and ^{231}Pa may reflect the rate of ligand scavenging from seawater, and provide constraints on ligand removal. In global iron models with dynamic ligands, the loss fluxes of ligands due to aggregation and/or scavenging are either completely unconstrained by data (Völker and Tagliabue, 2015) or not included (Misumi et al., 2013). While we prefer the interpretation that adsorption of ^{230}Th and ^{231}Pa occurs as a result of direct scavenging to metal oxides, we hesitate to rule out the role of ligands completely, and believe that the distribution of thorium isotopes might be used to understand some of the dynamic processes involved in hydrothermal iron-binding ligand production, aggregation, and destruction. One way this might be achieved is by analyzing hydrothermal particles for the concentrations and structures (e.g. Boiteau et al., 2013) of ligands present to determine if co-precipitation of metal oxide particles scavenges dissolved metal-binding ligands from solution. Another might be to apply the method used by Kipp et al. (this issue) to evaluate the loss rate of dissolved Fe to calculate the loss rate of dissolved L1 ligands across the GP16 section to determine the linkage between iron loss to particles with L1 ligand loss. Given their potential influence on trace metal scavenging and the stabilization of dissolved forms of iron, testing the destruction mechanisms of ligands in hydrothermal plumes would be a valuable topic for future work.

3.3. Where and when does scavenging occur?

Where scavenging occurs relative to the input of hydrothermal material is critical for understanding the local mass balance and sedimentary input of trace metals. Several studies have attempted to connect the concentrations of ^{230}Th and ^{231}Pa in ridge flank sediments to variations in hydrothermal activity through time (Frank et al., 1994; German et al., 1997, 1993; Lund and Asimow, 2011; Shimmield and Price, 1988). To better understand the effects of hydrothermal activity on the location of ^{230}Th and ^{231}Pa removal from the water column, we construct tracer-tracer plots of dissolved ^{3}He$_{xs}$ (Jenkins et al., this issue) with dissolved, particulate, and total ^{230}Th and ^{231}Pa (Fig. 11). Both tracers are shown in terms of inventories, integrated from 2200 to 2800 m. Similarly to Resing et al. (2015), our integrations at station 18 only go to 2640 m for ^{3}He$_{xs}$ and dissolved ^{230}Th and ^{231}Pa, and to 2610 m for particulate and total activities of ^{230}Th and ^{231}Pa. Since we lack particulate samples between 300 m and 2400 m depth at station 34, we do not calculate inventories of particulate or total ^{230}Th and ^{231}Pa there. With the exception of stations 18 and 23, the dissolved and total inventories of ^{230}Th and ^{231}Pa tend to increase (Fig. 11), while the particulate inventories of ^{230}Th and ^{231}Pa decrease at stations progressively further west of the EPR.

Tracer-tracer plots utilize curvature as a signal for scavenging and removal (German et al., 1991, 1990; Rudnicki and Elderfield, 1993). If an element or isotope forms a straight line with regard to a conservative tracer, then, disregarding potential changes in endmember tracer concentrations, mixing and dilution away from a hydrothermal source would be the only process accounting for the co-variation of the two elements. These relationships become more difficult for ^{230}Th and ^{231}Pa, which have multiple in-situ sources.

Ingrowth from uranium decay causes dissolved inventories of ^{230}Th and ^{231}Pa to increase away from the ridge axis as a function of plume age. Scavenging would act to lower the slope of that increase with time, and also add a significant source for the mass budget of particulate
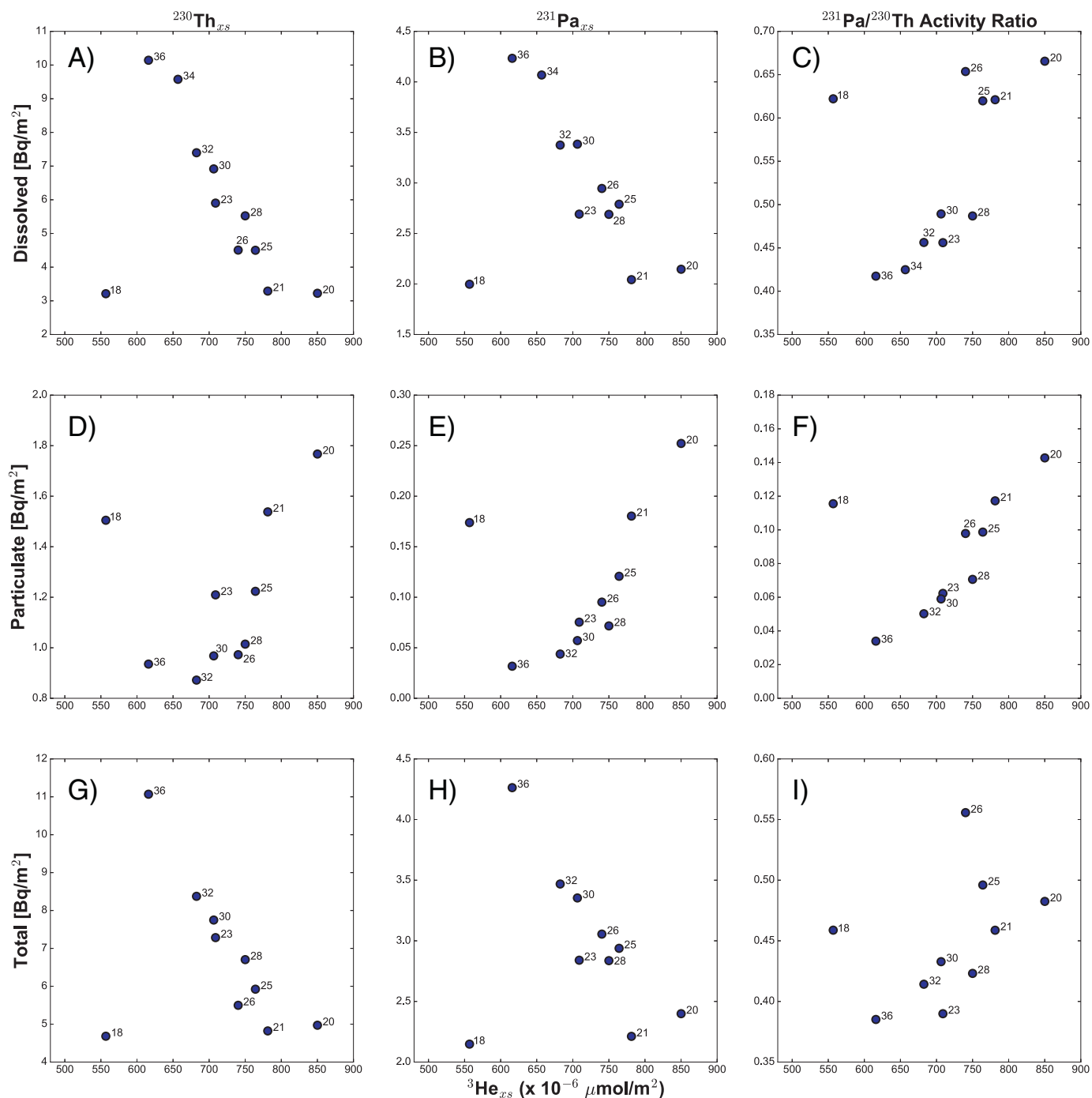
Fig. 11. Cross plots of radionuclide inventories (2200–2800 m depth interval) with hydrothermal [3]He (Jenkins et al., 2017). From left to right: ^{230}Th$_{xs}$, ^{231}Pa$_{xs}$, and xs ^{231}Pa/^{230}Th activity ratio. Top row: dissolved inventories. Middle row: Particulate inventories. Bottom row: total inventories.

plume inventories of ^{230}Th and ^{231}Pa. In addition, there is a net source of ^{230}Th and ^{231}Pa to the hydrothermal plume as it moves west via desorption from particles settling from the sea surface, which carry higher ^{230}Th and ^{231}Pa activities than the waters within the plume.

Particulate ^{230}Th and ^{231}Pa inventories are positively correlated with ^{3}He$_{xs}$, with the exception of station 18 (Fig. 11d–e). After station 20, the particulate radionuclide inventories decline rapidly towards station 21, then, with the exception of station 23 which is thought to be a recirculation feature that disrupts the continuous westward aging of the plume (Jenkins et al., this issue), decline towards station 36 with concave upward shape relative to ^{3}He$_{xs}$. If the particulate inventories were governed solely by adsorption of ^{230}Th and ^{231}Pa either ingrown

from uranium decay or desorbed from surface particles, we would expect their inventories to be convex upward with respect to ^{3}He$_{xs}$. Qualitatively, the concave upward relationships between ^{230}Th and ^{231}Pa inventories with ^{3}He$_{xs}$ (Fig. 11d–e) support continuous net removal of particulate ^{230}Th and ^{231}Pa throughout the plume.

We construct a simple mass balance to test whether dissolved ^{230}Th and ^{231}Pa are continuously scavenged over the entire area of the hydrothermal plume observed on GP16. To show net removal from the plume, we only need to prescribe two sources as the plume moves west: ingrowth by uranium decay and desorption from surface-derived particles falling into the hydrothermal plume. Not included is dilution of plume waters by mixing, an issue we will return to later.

While the production rate of ^{230}Th and ^{231}Pa by uranium decay is well-known, it is not straightforward to calculate the desorption flux of ^{230}Th and ^{231}Pa from sinking surface-derived particles. These particles are in equilibrium with respect to adsorption and desorption with waters directly above the plume, which have higher dissolved ^{230}Th and ^{231}Pa concentrations than in the plume. Thus, to come into equilibrium within the plume, the surface-derived particles will lose Th and Pa to the dissolved phase via desorption. We estimate the net supply of dissolved ^{230}Th and ^{231}Pa by desorption as the difference between the flux of particulate ^{230}Th and ^{231}Pa falling into the plume on surface-derived particles and the flux of particulate ^{230}Th and ^{231}Pa leaving the plume on surface-derived particles.

Given previous estimates of desorption rate constants for thorium of 0.1–10 yr^{-1} (Bacon and Anderson, 1982; Lerner et al., 2016; Murnane et al., 1994) and bulk particle sinking rates of 300–900 m/yr (Lerner et al., 2016), we infer that the entire flux of particulate ^{230}Th and ^{231}Pa is desorbed at least once during the lifetime of surface-derived particles within the hydrothermal plume. Away from features that lead to convergence or divergence of the lateral flux of ^{230}Th and ^{231}Pa by mixing, such as boundary scavenging, and given a uniform particle field, the downward flux (F) of particulate ^{230}Th and ^{231}Pa through any depth horizon (z) is equal to the integrated production by uranium decay in the overlying water column:

$$F_z = \beta^* z \tag{5}$$

Here, β is the known production rate of ^{230}Th or ^{231}Pa, in units of activity/m^2/yr. We can treat the integrated production in the overlying water column as the source term for gross desorption of particulate ^{230}Th and ^{231}Pa from surface-derived particles.

Adsorption of dissolved ^{230}Th and ^{231}Pa onto surface-derived particles will also occur within the hydrothermal plume. Net desorption must be estimated as the difference between supply of dissolved ^{230}Th by desorption from surface-derived particles and loss by adsorption onto them and subsequent sedimentation. Eq. (5) provides a way to calculate the sinking flux of particulate ^{230}Th and ^{231}Pa into the plume. With reversible scavenging, F_z is also directly proportional to the activity of dissolved ^{230}Th or ^{231}Pa at the depth z, A_z:

$$F_z = A_z^* U \tag{6}$$

U is a constant proportional to particle flux, in units m/yr. Assuming for now that there is no change in the properties of surface-derived particles as they fall through the hydrothermal plume, we can evaluate the adsorption of dissolved ^{230}Th and ^{231}Pa at the depth of their minimum dissolved activities as:

$$F_{min} = A_{min}^* U \tag{7}$$

To calculate F_{min}, we first determine the value of U above the plume by combining Eq. (5) and Eq. (6) at the depth of 2200 m:

$$F_{2200} = \beta^* 2200 = A_{2200}^* U \tag{8}$$

Rearranging, we solve for U as:

$$U = \frac{\beta^* 2200}{A_{2200}} \tag{9}$$

After having solved for U, we can solve for the loss of dissolved ^{230}Th and ^{231}Pa from the plume by adsorption onto surface-derived particles using Eq. (7). The net supply of ^{230}Th and ^{231}Pa (F$_{des}$, units activity/m^2/yr) within the plume by desorption from surface-derived particles, at each station, is then:

$$F_{des} = F_{2200} - F_{min} \tag{10}$$

Before continuing to the mass balance, we return to our assumption that the adsorptive capabilities of surface-derived particles do not change within the depth range of the plume. In fact, surface particles are likely to be coated by precipitating Fe(OH)$_3$ and/or MnO$_2$ during their transit, as described in Section 3.2.2, which would alter the

sorptive properties of surface functional groups on the particles. However, we can conceptually treat Fe(OH)$_3$ and MnO$_2$ coatings on surface-derived particles as plume particles. As a result, our assumption of no change in the adsorptive properties of surface-derived particles represents an upper limit to their contribution to scavenging loss of ^{230}Th and ^{231}Pa from the hydrothermal plume. In our overall mass balance within the plume, removal of ^{230}Th and ^{231}Pa would therefore be a minimum estimate.

We can write a mass balance for the inventories (I, units Bq/m^2) of ^{230}Th and ^{231}Pa within the hydrothermal plume as follows:

$$\frac{dI}{dt} = \beta + F_{des} - F_{scav} \tag{11}$$

β is the production rate from uranium decay integrated across 600 m and F$_{des}$ is the net desorption flux from surface-derived particles into the hydrothermal plume. Both of these components have units of Bq/m^2/yr. We can calculate the change in time (dt) between stations by dividing the westward distance component (Δx) between each station by a water mass velocity (v) of 0.4 cm/s (Hautala and Riser, 1993). After discretizing and rearranging, our final mass balance model for the westward evolution of ^{230}Th and ^{231}Pa in the hydrothermal plume can be written:

$$I_{stn} = I_{prev} + (\beta + F_{des})^* \frac{\Delta x}{v} \tag{12}$$

I$_{stn}$ is the modeled inventory of ^{230}Th or ^{231}Pa being solved for at a given station, and I$_{prev}$ is the modeled inventory at the closest station to the east. Before discussing the results of the model, it is critical to acknowledge that we purposefully neglect mixing as a source of ^{230}Th and ^{231}Pa to the hydrothermal plume. Mixing of depleted plume waters with ambient, non-plume deep water would serve as a third source of ^{230}Th and ^{231}Pa. However, we cannot adequately constrain the rates of mixing. Therefore, for our preliminary mass balance, we leave out the effects of mixing.

We find that, for ^{230}Th, production alone slightly over predicts the observed inventories of ^{230}Th west of the EPR (Fig. 12). With desorption added in, the modeled ^{230}Th inventories are much greater than the observed inventories. This means that continuous scavenging onto plume-derived particles must be happening within the hydrothermal plume, sufficient to balance desorption of ^{230}Th from particles falling in from above and any other sources of Th to the hydrothermal plume, such as mixing with non-plume waters, which would serve as a net source. As a result, the amount of ^{230}Th falling to the sediments beneath stations west of the EPR would roughly balance production in the entire overlying water column. Our model therefore indicates that in sediments hundreds to thousands of kilometers downstream of hydrothermal venting, the use of ^{230}Th as a constant flux proxy for deriving sediment mass accumulation rates (e.g. Francois, 2004) is valid. For ^{231}Pa, production alone cannot account for the increase moving west of the EPR. Only after the desorption flux is added does the modeled ^{231}Pa become greater than the observed inventories. The hydrothermal scavenging removal of ^{231}Pa is thus less than the desorption flux, and the amount of ^{231}Pa reaching the sediments would be less than production in the entire overlying water column.

3.4. Differential scavenging behavior of ^{232}Th

Until now, our discussion of the behavior in thorium in the hydrothermal plume observed on GP16 has focused on radiogenic ^{230}Th. It is generally assumed that, since they have the same valence shell, neither has a known biological use, and thorium does not participate in redox reactions, the scavenging dynamics of ^{232}Th and ^{230}Th should be identical. This assumption is critical in applying the removal residence time derived from measuring ^{230}Th to ^{232}Th for calculating dust fluxes (Deng et al., 2014; Hayes et al., 2015c, 2013a; Lopez et al., 2015), boundary exchange fluxes (Hayes et al., 2013a), and potentially to
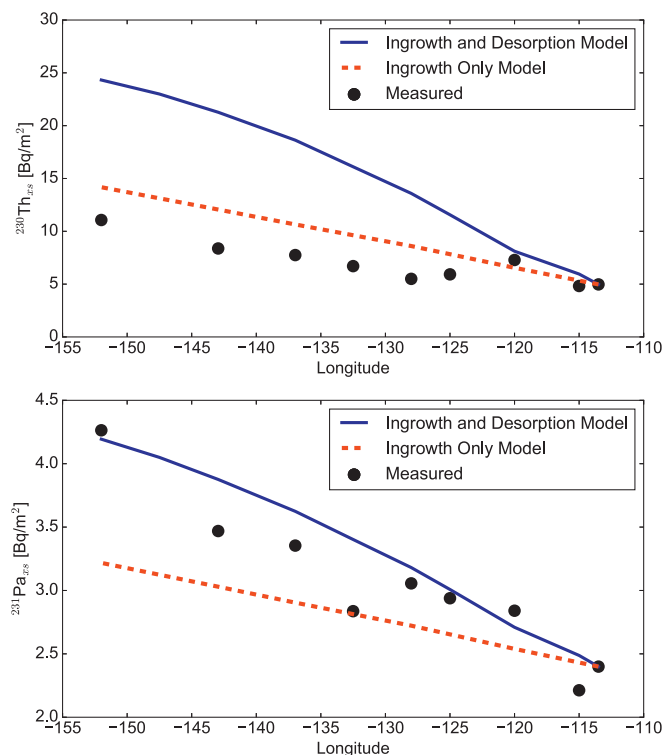
Fig. 12. Mass Balance Modeled and Observed Inventories of ^{230}Th and ^{231}Pa at stations west of the EPR. Red dashed lines show models with ingrowth from uranium decay as the only source, and solid blue lines show models with additional desorption flux. (For interpretation of the references to colour in this figure legend, the reader is referred to the web version of this article.)

Fig. 13. Dissolved ^{232}Th/^{230}Th atom ratio at stations west of the EPR ridge axis on GP16. Error bars represent 1-sigma uncertainty, and errors are smaller than the symbol size where not visible.

benthic nepheloid layers (Bacon and Rutgers van der Loeff, 1989; Rutgers van der Loeff et al., 2002). Differential incorporation into colloids has been proposed as a potential mechanism by which to fractionate ^{232}Th from ^{230}Th; however, the only studies with measurements of colloidal ^{232}Th and ^{230}Th have found that both isotopes have a similar fraction of their dissolved concentration as colloids (Hayes et al., 2015c, 2017; Roy-Barman et al., 2002). For particle-reactive nuclides like ^{232}Th with surface and ocean bottom sources, rather than an in-situ source from radioactive decay, the 1-d profile expected from reversible scavenging would be a constant value throughout the water column (Bacon and Anderson, 1982). Reversibly scavenged nuclides with in-situ sources from uranium decay (^{230}Th, ^{231}Pa) would be expected to increase linearly with depth (Bacon and Anderson, 1982). Therefore, under reversible scavenging conditions, the ^{232}Th/^{230}Th ratio would decrease with depth. Typically, ^{232}Th concentrations are constant below 1000 m (Hayes et al., 2013a), meaning that decreases in the ^{232}Th/^{230}Th ratio due to reversible scavenging are observed below that depth. If ^{232}Th and ^{230}Th were scavenged identically in the GP16 hydrothermal plume, then we would expect that the observed trend of decreasing ^{232}Th/^{230}Th with depth in the overlying water column would continue through the plume.

On GP16, the dissolved ^{232}Th/^{230}Th ratio decreases slightly throughout the water column from 1000 to 2000 m depth, as expected from reversible scavenging, before rapidly increasing to a maximum within the hydrothermal plume (Fig. 13). The highest plume ^{232}Th/^{230}Th ratios are observed at stations closest to the ridge axis, with ^{232}Th/^{230}Th ratios decreasing westward, with the exception of a high ^{232}Th/^{230}Th ratio observed at station 26 (Fig. 13). The maximum in ^{232}Th/^{230}Th ratio likely reflects a plume source of dissolved ^{232}Th that reacts differently with particles compared to ^{230}Th. We can test this hypothesis by calculating the amount of additional ^{232}Th in the plume compared to what is expected from reversible scavenging (Fig. 4b). In
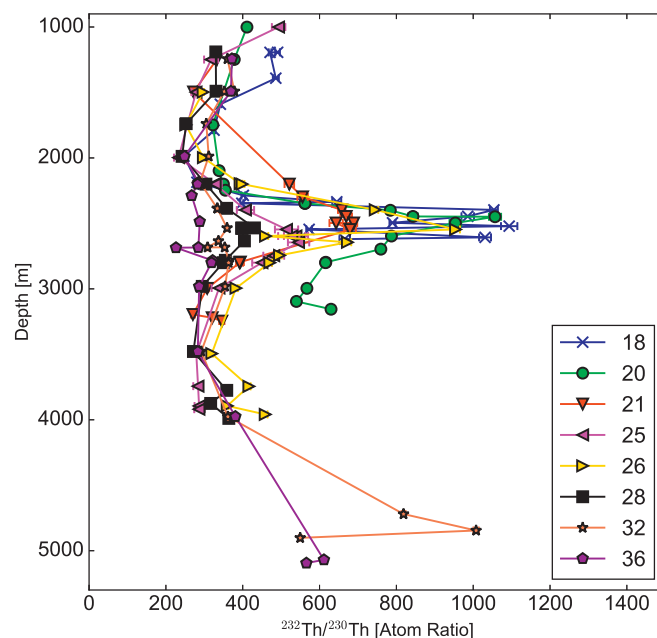
the presence of intense scavenging in the hydrothermal plume, we would expect ^{232}Th to experience the same degree of depletion, relative to reversible scavenging, as ^{230}Th does. To calculate the amount of additional unreactive ^{232}Th added in the hydrothermal plume, we first determine the expected concentration of ^{232}Th if it experienced the same degree of scavenging as ^{230}Th:

$$^{232}Th_{exp} = {}^{232}Th_{rev}*(1 - \%\text{depletion}) \tag{13}$$

^{232}Th$_{rev}$ is defined as the concentration of dissolved ^{232}Th expected from reversible scavenging. We use the concentration of ^{232}Th at 2200 m depth at each station, just above the hydrothermal plume, as the value for ^{232}Th$_{rev}$. The % depletion term is derived from the % depletion calculated using Eq. (1), but with dissolved instead of total ^{230}Th$_{xs}$. We then integrate the measurements of dissolved ^{232}Th (^{232}Th$_{meas}$) within the hydrothermal plume at each station to calculate the observed inventory of ^{232}Th (^{232}Th$_{obs}$) present within the plume:

$$^{232}Th_{obs} = \int_{2200}^{2800} {}^{232}Th_{meas}dz \tag{14}$$

The extra ^{232}Th (^{232}Th$_{add}$) is simply the difference between the observed inventory of ^{232}Th and the amount expected from reversible scavenging:

$$^{232}Th_{add} = {}^{232}Th_{obs} - {}^{232}Th_{exp} \tag{15}$$

Stations with low (high) ^{232}Th$_{add}$ would have high (low) observed ^{232}Th, low (high) ^{232}Th at 2200 m, or high (low) percent depletion of ^{230}Th.

If our hypothesis that ^{232}Th$_{add}$ reflects an unreactive hydrothermal ^{232}Th source is correct, then we would expect to see that it has a constant, positively correlated slope with ^{3}He$_{xs}$, with decreasing concentrations of both moving away from the ridge axis. An unreactive pool of dissolved ^{232}Th would have to be stabilized in the colloidal phase. Colloids are still removed by aggregation and sinking, so if the ^{232}Th$_{add}$/^{3}He$_{xs}$ ratio decreased across the transect, with a maximum near the ridge axis, then this might indicate ^{232}Th in a colloidal phase undergoing aggregation and removal from the dissolved phase. With the exception of station 26, which had unexpectedly high ^{232}Th/^{230}Th ratios within the plume, ^{232}Th$_{add}$ decreases linearly away from the
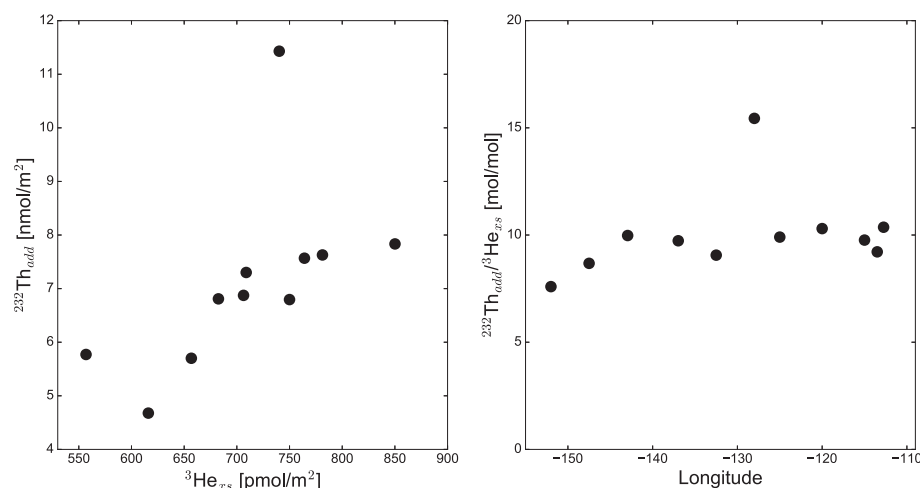
Fig. 14. A) Hydrothermal-sourced $^{232}Th_{add}$ inventories plotted against hydrothermal ^3He ($^3He_{xs}$) inventory within the plume (2200–2800 m depth interval). Each point corresponds to a full-depth station (Fig. 1). B) $^{232}Th_{add}/^3He_{xs}$ inventory ratios plotted against longitude, showing a nearly constant ratio between stations 18–32 (except 26), before decreasing at stations 34 and 36.
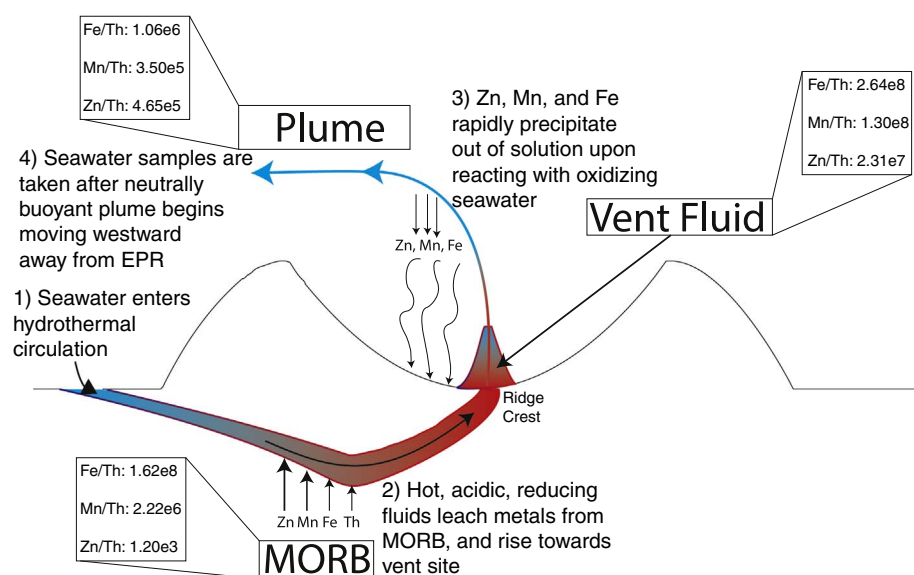

Fig. 15. Cartoon illustrating the movement of trace metals through different reservoirs (MORB, vent fluids, deep ocean hydrothermal plume) during hydrothermal circulation. Me/Th values (mol/mol) are shown for n-MORB (Gale et al., 2013), vent fluids (Chen, 1987; Chen et al., 1986), and flux ratios from the hydrothermal plume observed on GP16 Eq. (16).

ridge axis from stations 18–32 (Fig. 14a), with a constant ratio to $^3He_{xs}$ (Fig. 14b). We believe this is strong evidence for a ridge crest source of unreactive, colloidal ^{232}Th. Interestingly, there is a decrease in the $^{232}Th_{add}/^3He_{xs}$ ratio at stations 34 and 36 (Fig. 14b). This may reflect an increase in the aggregation and removal rate of the ^{232}Th-binding colloids, more efficient scavenging of colloids by greater biogenic particle flux raining into the plume from the overlying water column (Black et al., this issue), or second-order reaction kinetics of colloid aggregation.

Assuming that the constant $^{232}Th_{add}/^3He_{xs}$ ratio reflects the ratio being erupted at the ridge axis, we can determine the flux of hydrothermal ^{232}Th to the oceans. We regress $^{232}Th_{add}$ against $^3He_{xs}$, for stations 20–32, not including station 26 (n = 7), to find a $^{232}Th_{add}/^3He_{xs}$ ratio of 7.14 ± 1.17 (1σ standard deviation) mol/mol. There are many estimates of the global ^3He flux (Bianchi et al., 2010; Craig et al., 1975; Dutay et al., 2004; Schlitzer, 2016), but for ease of comparison to other data (Resing et al., 2015; Roshan et al., 2016) from GP16, we use the 527 ± 102 mol yr^{-1} estimate of Bianchi et al. (2010). Multiplying the $^{232}Th_{add}/^3He_{xs}$ ratio found on GP16 by the global ^3He flux allows us to calculate the global ^{232}Th flux from hydrothermal vents, which we find to be 3760 ± 950 mol yr^{-1}. Using a global dust deposition to the oceans of 450 Tg yr^{-1} (Jickells et al., 2005), 14 ppm ^{232}Th in the < 5 μm fraction of dust source sediments (Kienast et al., 2016; McGee et al., 2016), and an estimate of the

solubility of ^{232}Th as 15% (Deng et al., 2014; Hayes et al., 2013a), we calculate a global input rate of dissolved ^{232}Th from dust of 4.07×10^6 moles yr^{-1}. The hydrothermal flux of operationally defined dissolved, but actually unreactive colloidal ^{232}Th is < 1% of the dissolved ^{232}Th flux from dust, meaning that hydrothermal inputs constitute a negligible portion of the oceanic thorium budget.

The inferred flux of hydrothermal ^{232}Th can be compared to those calculated for Fe, Mn (Resing et al., 2015) and Zn (Roshan et al., 2016) from GP16 data. For each metal (Me), the flux is computed by multiplying the water column Me/$^3He_{xs}$ ratio by the global $^3He_{xs}$ flux (as done for $^{232}Th_{add}$ in the previous paragraph). By taking the ratio of these fluxes to the flux of $^{232}Th_{add}$, the $^3He_{xs}$ terms cancel and we are left with the flux ratio of Fe, Mn, or Zn to $^{232}Th_{add}$ (Me/Th):

$$\text{Me/Th flux ratio} = \frac{\text{Me}^{\text{Flux}}}{^{232}\text{Th}_{\text{add}}^{\text{flux}}} = \frac{\text{Me}/^3\text{He}_{xs}}{^{232}\text{Th}_{\text{add}}/^3\text{He}_{xs}} \tag{16}$$

If the colloids maintaining $^{232}Th_{add}$ in the dissolved phase are basaltic in origin, we might expect that the Fe/$^{232}Th_{add}$, Mn/$^{232}Th_{add}$, and Zn/$^{232}Th_{add}$ (together denoted Me/Th, with units mol/mol) flux ratios on GP16 are similar to the ratios found in average n-MORB (Gale et al., 2013), or to the ratios found in endmember hydrothermal vent fluids, though there are few (n = 7) measurements of ^{232}Th concentration in vent fluids (Chen, 1987; Chen et al., 1986). To determine the mobility

of these three metals relative to thorium in different stages of hydrothermal circulation, we compare the Me/Th ratios from n-MORB to hydrothermal fluids, and the Me/Th ratios of hydrothermal fluids to the dissolved Me/Th flux ratios from water column measurements in the hydrothermal plume sampled on GP16 (Fig. 15). As hydrothermal circulation begins, seawater is heated and passes through the ocean crust (part 1 in Fig. 15). This hot, acidic, reducing water leaches metals from the ocean crust, and becomes buoyant enough to rise towards the surface as the fluid in hydrothermal vents (part 2 in Fig. 15). By comparing the Me/Th ratios in vent fluids with Me/Th in the ocean crust, we test the relative mobility of trace metals to thorium under the conditions of hydrothermal circulation. In hydrothermal fluids, Fe/Th is 1.5 times higher than in n-MORB, Mn/Th is 50 times higher than in n-MORB, and Zn/Th is 20,000 times higher than in n-MORB. Zn is known to be strongly enriched in hydrothermal fluids over MORB (Von Damm et al., 1985), which drives the much greater Zn/Th ratio in fluids compared to n-MORB. The similar Fe/Th values in both fluids and n-MORB indicate that Fe and Th have similar mobility under the hot, reducing, acidic conditions under which metals are leached from ocean crust.

Vent fluids then erupt and vigorously mix with ambient seawater, resulting in the precipitation of metals as sulfides and/or oxyhydroxides (part 3 in Fig. 15). By comparing water column Me/Th flux ratios from GP16 with those in vent fluids, we can evaluate the relative reactivity of Fe, Mn, and Zn compared to ^{232}Th between the time of eruption and subsequent rising, mixing, and westward transit as a neutrally buoyant plume (part 4 in Fig. 14). The dissolved Zn/Th flux ratio in the hydrothermal plume is 50 times lower than the Zn/Th ratio in hydrothermal fluids; the Fe/Th plume flux ratio is 250 times lower than in the Fe/Th of vent fluids; and the Mn/Th flux ratio is 370 times lower than the Mn/Th of vent fluids. Given that Fe and Zn are thought to rapidly precipitate out of solution as sulfides upon being erupted and reacting with seawater, it is surprising that the dissolved Zn/Th flux ratio in seawater is most enriched compared to vent fluids, and the Mn/Th ratio is the most depleted compared to vent fluids. This could reflect spatio-temporal variations in vent fluid chemistry (e.g. Yücel and Luther, 2013), for example, if the endmember vent fluids from the Juan de Fuca Ridge and the EPR at 21°N used to represent vent fluid chemistry have different Fe, Mn, and Zn concentrations than those being erupted at 15–17°S on the EPR, which feed the hydrothermal plume sampled on GP16. Regardless of the pattern, Fe, Mn, and Zn are removed from solution much faster than ^{232}Th$_{add}$ upon reacting with seawater.

Since ^{232}Th$_{add}$ is in excess of what is expected from ^{230}Th scavenging, it is unlikely that the formation of ^{232}Th-binding colloids happens within the water column, since those processes would likely bind ^{230}Th as well and link the scavenging behavior of the two isotopes. Given the high affinity of dissolved Th for adsorption to MnO_2 and $Fe(OH)_3$, if ^{232}Th were erupted in dissolved form, then it should have been scavenged immediately after eruption by the rapidly forming Mn and Fe oxides. If we assume that all of the ^{232}Th$_{add}$ is released in the form of unreactive basaltic colloids, then the low Me/Th flux ratios compared to the Me/Th ratios of vent fluids would indicate that only a small fraction of dissolved Fe, Mn, and Zn are released into the water column in the same unreactive phase as Th, since if they were, the water column Me/Th ratios would be expected to stay similar to the vent fluid Me/Th ratios. Though circumstantial, we take this to be evidence that the high percentage of colloidal Fe found in hydrothermal plumes (Fitzsimmons et al., 2014) is likely bound into colloids well after being erupted into oxidizing seawater.

4. Summary and conclusions

The isotopes of thorium and protactinium offer unique insights into trace metal scavenging by hydrothermal plumes particles. Deficits in the dissolved and total activities of ^{230}Th and ^{231}Pa within the plume were observed 4000 km away from the EPR ridge crest, indicating basin-scale signatures of hydrothermal scavenging. The timescales over

which these signatures will be preserved after waters pass beyond locations of hydrothermal activity are 64 years for ^{230}Th and 140 years for ^{231}Pa. While we cannot rule out the potential co-precipitation of Th- and Pa- binding ligands as the driver of scavenging, the tight co-variation of Mn and $Fe(OH)_3$ particles and the distribution coefficients and fractionation factors of ^{230}Th and ^{231}Pa lead us to conclude that direct adsorption to nanoparticulate metal surface sites is the mechanism for ^{230}Th and ^{231}Pa scavenging in the hydrothermal plume. A mass balance model for the westward evolution of the hydrothermal plume requires continuous removal of ^{230}Th and ^{231}Pa. For ^{230}Th, removal balances sources other than production, such as desorption from surface-derived particles, and the amount of ^{230}Th reaching the seafloor below the plume should be equal to production in the overlying water column. Unlike ^{230}Th, hydrothermally-derived ^{232}Th is not as efficiently scavenged within the dissolved phase, indicating a hydrothermal source of ^{232}Th that is likely bound in an unreactive colloidal phase. In all of these cases, we raised several questions about the details of the scavenging, speciation, and particle dynamics that could potentially be answered by improved analytical techniques for measuring colloidal Th and Pa, future GEOTRACES sections, and future process studies.

References

Andersen, M.B., Stirling, C.H., Zimmermann, B., Halliday, A.N., 2010. Precise determination of the open ocean 234U/238U composition. Geochem. Geophys. Geosyst. 11 n/a–n/a. http://dx.doi.org/10.1029/2010GC003318.

Anderson, R.F., Bacon, M.P., Brewer, P.G., 1983a. Removal of 230Th and 231Pa from the open ocean. Earth Planet. Sci. Lett. 62, 7–23. http://dx.doi.org/10.1016/0012-821X(83)90067-5.

Anderson, R.F., Bacon, M.P., Brewer, P.G., 1983b. Removal of 230Th and 231Pa at ocean margins. Earth Planet. Sci. Lett. 66, 73–90. http://dx.doi.org/10.1016/0012-821X(83)90127-9.

Anderson, R.F., Fleisher, M.Q., Robinson, L.F., Edwards, L.R., Hoff, J.A., Moran, S.B., Rutgers van der Loeff, M.M., Thomas, A., Roy-Barman, M., François, R., 2012. GEOTRACES Intercalibration of 230Th, 232Th, 231Pa and prospects for 10Be. Limnol. Oceanogr. Methods 10, 179–213. http://dx.doi.org/10.4319/lom.2012.10.179.

Bacon, M.P., Anderson, R.F., 1982. Distribution of thorium isotopes between dissolved and particulate forms in the Deep Sea. J. Geophys. Res. 87, 2045–2056. http://dx.doi.org/10.1111/j.1365-3091.2012.01327.x.

Bacon, M.P., Rutgers van der Loeff, M.M., 1989. Removal of thorium-234 by scavenging in the bottom nepheloid layer of the ocean. Earth Planet. Sci. Lett. 92, 157–164. http://dx.doi.org/10.1016/0012-821X(89)90043-5.

Balistrieri, L.S., Murray, J.W., 1986. The surface chemistry of sediments from the Panama Basin: the influence of Mn oxides on metal adsorption. Geochim. Cosmochim. Acta 50, 2235–2243. http://dx.doi.org/10.1016/0016-7037(86)90078-5.

Barbeau, K., Kujawinski, E.B., Moffett, J.W., 2001. Remineralization and recycling of iron, thorium and organic carbon by heterotrophic marine protists in culture. Aquat. Microb. Ecol. 24, 69–81.

Bennett, S.A., Achterberg, E.P., Connelly, D.P., Statham, P.J., Fones, G.R., German, C.R., 2008. The distribution and stabilisation of dissolved Fe in deep-sea hydrothermal plumes. Earth Planet. Sci. Lett. 270, 157–167. http://dx.doi.org/10.1016/j.epsl.2008.01.048.

Bianchi, D., Sarmiento, J.L., Gnanadesikan, A., Key, R.M., Schlosser, P., Newton, R., 2010. Low helium flux from the mantle inferred from simulations of oceanic helium isotope data. Earth Planet. Sci. Lett. 297, 379–386. http://dx.doi.org/10.1016/j.epsl.2010.06.037.

Black, E.E., Buesseler, K., Pike, S., Lam, P.J., 2017. 234Th as a tracer of particulate export and remineralization in the southeastern tropical Pacific. Mar. Chem (this issue).

Boiteau, R.M., Fitzsimmons, J.N., Repeta, D.J., Boyle, E.A., 2013. Detection of iron ligands in seawater and marine cyanobacteria cultures by high-performance liquid chromatography–inductively coupled plasma-mass spectrometry. Anal. Chem. http://dx.doi.org/10.1021/ac3034568.

Boström, K., Peterson, M.N.A., Joensuu, O., Fisher, D.E., 1969. Aluminum-poor ferro-manganoan sediments on active oceanic ridges. J. Geophys. Res. Oceans 74, 3261–3270. http://dx.doi.org/10.1029/JB074i012p03261.

Buck, K.N., Sohst, B., Sedwick, P.N., 2015. The organic complexation of dissolved iron along the U.S. GEOTRACES (GA03) North Atlantic Section. Deep-Sea Res. II Top. Stud. Oceanogr. 116, 152–165. http://dx.doi.org/10.1016/j.dsr2.2014.11.016.

Chase, Z., Anderson, R.F., Fleisher, M.Q., 2002. The influence of particle composition and particle flux on scavenging of Th, Pa and Be in the ocean. Earth Planet. Sci. Lett. 204, 214–229.

Chen, J.H., 1987. U, Th, and Pb isotopes in hot springs on the Juan de Fuca Ridge. J. Geophy. Res. Oceans 92, 11411–11415. http://dx.doi.org/10.1029/JB092iB11p11411.

Chen, J.H., Wasserburg, G.J., Von Damm, K.L., Edmond, J.M., 1986. The U-Th-Pb systematics in hot springs on the East Pacific Rise at 21°N and Guaymas Basin. Geochim. Cosmochim. Acta 50, 2467–2479. http://dx.doi.org/10.1016/0016-7037(86)90030-X.

Cheng, H., Lawrence Edwards, R., Shen, C.-C., Polyak, V.J., Asmerom, Y., Woodhead, J., Hellstrom, J., Wang, Y., Kong, X., Spötl, C., Wang, X., Calvin Alexander Jr., E., 2013. Improvements in 230Th dating, 230Th and 234U half-life values, and U–Th isotopic measurements by multi-collector inductively coupled plasma mass spectrometry. Earth Planet. Sci. Lett. 371-372, 82–91. http://dx.doi.org/10.1016/j.epsl.2013.04.006.

Cowen, J.P., Bruland, K.W., 1985. Metal deposits associated with bacteria: implications for Fe and Mn marine biogeochemistry. Deep Sea Research Part A. Oceanogr. Res. Pap. 32, 253–272. http://dx.doi.org/10.1016/0198-0149(85)90078-0.

Cowen, J.P., Massoth, G.J., Baker, E.T., 1986. Bacterial scavenging of Mn and Fe in a mid-to far-field hydrothermal particle plume. Nature 322, 169–171. http://dx.doi.org/10.1038/322169a0.

Cowen, J.P., Massoth, G.J., Feely, R.A., 1990. Scavenging rates of dissolved manganese in a hydrothermal vent plume. Deep Sea Research Part A. Oceanogr. Res. Pap. 37, 1619–1637. http://dx.doi.org/10.1016/0198-0149(90)90065-4.

Craig, H., Clarke, W.B., Beg, M.A., 1975. Excess 3He in deep water on the East Pacific rise. Earth Planet. Sci. Lett. 26, 125–132. http://dx.doi.org/10.1016/0012-821X(75)90079-5.

Deng, F., Thomas, A.L., Rijkenberg, M.J.A., Henderson, G.M., 2014. Controls on seawater 231Pa, 230Th and 232Th concentrations along the flow paths of deep waters in the Southwest Atlantic. Earth Planet. Sci. Lett. 390, 93–102. http://dx.doi.org/10.1016/j.epsl.2013.12.038.

Dutay, J.C., Jean-Baptiste, P., Campin, J.M., Ishida, A., Maier-Reimer, E., Matear, R.J., Mouchet, A., Totterdell, I.J., Yamanaka, Y., Rodgers, K., Madec, G., Orr, J.C., 2004. Evaluation of OCMIP-2 ocean models' deep circulation with mantle helium-3. J. Mar. Syst. 48, 15–36. http://dx.doi.org/10.1016/j.jmarsys.2003.05.010.

Estapa, M.L., Breier, J.A., German, C.R., 2015. Particle dynamics in the rising plume at Piccard Hydrothermal Field, Mid-Cayman Rise. Geochem. Geophys. Geosyst. 16, 2762–2774. http://dx.doi.org/10.1002/2015GC005831.

Falkowski, P.G., Barber, R.T., Smetacek, V., 1998. Biogeochemical controls and feedbacks on ocean primary production. Science 281, 200–206. http://dx.doi.org/10.1126/science.281.5374.200.

Faure, V., Speer, K., 2012. Deep circulation in the Eastern South Pacific Ocean. J. Mar. Res. 70, 748–778. http://dx.doi.org/10.1357/002224012806290714.

Feely, R.A., Lewison, M., Massoth, G.J., Robert Baldo, G., Lavelle, J.W., Byrne, R.H., Von Damm, K.L., Curl, H.C., 1987. Composition and dissolution of black smoker particulates from active vents on the Juan de Fuca Ridge. J. Geophys. Res. Oceans 92, 11347–11363. http://dx.doi.org/10.1029/JB092iB11p11347.

Feely, R.A., Baker, E.T., Marumo, K., Urabe, T., Ishibashi, J., Gendron, J., Lebon, G.T., Okamura, K., 1996. Hydrothermal plume particles and dissolved phosphate over the superfast-spreading southern East Pacific Rise. Geochim. Cosmochim. Acta 60, 2297–2323. http://dx.doi.org/10.1016/0016-7037(96)00099-3.

Field, M.P., Sherrell, R.M., 2000. Dissolved and particulate Fe in a hydrothermal plume at 9°45′N, East Pacific Rise. Geochim. Cosmochim. Acta 64, 619–628. http://dx.doi.org/10.1016/S0016-7037(99)00333-6.

Fitzsimmons, J.N., Boyle, E.A., Jenkins, W.J., 2014. Distal transport of dissolved hydrothermal iron in the deep South Pacific Ocean. Proc. Natl. Acad. Sci. U. S. A. 111, 16654–16661. http://dx.doi.org/10.1073/pnas.1418778111.

Fitzsimmons, J.N., John, S.G., Marsay, C.M., Hoffman, C.L., Nicholas, S.L., Toner, B.M., German, C.R., Sherrell, R.M., 2017. Iron persistence in a distal hydrothermal plume supported by dissolved-particulate exchange. Nat. Geosci. 10, 195–201. http://dx.doi.org/10.1038/ngeo2900.

Francois, R., 2004. 230Th normalization: an essential tool for interpreting sedimentary fluxes during the late Quaternary. Paleoceanography 19, PA1018. http://dx.doi.org/10.1029/2003PA000939.

Frank, M., Eckhardt, J.D., Eisenhauer, A., Kubik, P.W., Dittrich Hannen, B., Segl, M., Mangini, A., 1994. Beryllium 10, thorium 230, and protactinium 231 in Galapagos microplate sediments: implications of hydrothermal activity and paleoproductivity changes during the last 100,000 years. Paleoceanography 9, 559–578. http://dx.doi.org/10.1029/94PA01132.

Gale, A., Dalton, C.A., Langmuir, C.H., Su, Y., Schilling, J.G., 2013. The mean composition of ocean ridge basalts. Geochem. Geophys. Geosyst. 14, 489–518. http://dx.doi.org/10.1029/2012GC004334.

Geibert, W., Usbeck, R., 2004. Adsorption of thorium and protactinium onto different particle types: experimental findings. Geochim. Cosmochim. Acta 68, 1489–1501. http://dx.doi.org/10.1016/j.gca.2003.10.011.

German, C.R., Seyfried, W.E., 2014. Hydrothermal Processes. In: Holland, H.D., Turekian, K.K. (Eds.), Treatise on Geochemistry. Elsevier Ltd., pp. 191–233. http://dx.doi.org/10.1016/B978-0-08-095975-7.00607-0.

German, C.R., Klinkhammer, G.P., Edmond, J.M., Mura, A., Elderfield, H., 1990.

Hydrothermal scavenging of rare-earth elements in the ocean. Nature 345, 516–518. http://dx.doi.org/10.1038/345516a0.

German, C.R., Fleer, A.P., Bacon, M.P., Edmond, J.M., 1991. Hydrothermal scavenging at the Mid-Atlantic Ridge: radionuclide distributions. Earth Planet. Sci. Lett. 105, 170–181. http://dx.doi.org/10.1016/0012-821X(91)90128-5.

German, C.R., Higgs, N.C., Thomson, J., Mills, R., Elderfield, H., Blusztajn, J., Fleer, A.P., Bacon, M.P., 1993. A geochemical study of metalliferous sediment from the TAG Hydrothermal Mound, 26°08′N, Mid-Atlantic Ridge. J. Geophys. Res. Oceans 98, 9683–9692. http://dx.doi.org/10.1029/92JB01705.

German, C.R., Bourles, D.L., Brown, E.T., Hergt, J., Colley, S., Higgs, N.C., Ludford, E.M., Nelsen, T.A., Feely, R.A., Raisbeck, G., Yiou, F., 1997. Hydrothermal scavenging on the Juan de Fuca Ridge: 230Thxs, 10Be, and REEs in ridge-flank sediments. Geochim. Cosmochim. Acta 61, 4067–4078. http://dx.doi.org/10.1016/S0016-7037(97)00230-5.

German, C.R., Colley, S., Palmer, M.R., Khripounoff, A., Klinkhammer, G.P., 2002. Hydrothermal plume-particle fluxes at 13°N on the East Pacific Rise. Deep-Sea Res. I Oceanogr. Res. Pap. 49, 1921–1940. http://dx.doi.org/10.1016/S0967-0637(02)00086-9.

Hatta, M., Measures, C.I., Wu, J., Roshan, S., Fitzsimmons, J.N., Sedwick, P., Morton, P., 2015. An overview of dissolved Fe and Mn distributions during the 2010–2011 U.S. GEOTRACES north Atlantic cruises: GEOTRACES GA03. Deep-Sea Res. II Top. Stud. Oceanogr. 116, 117–129. http://dx.doi.org/10.1016/j.dsr2.2014.07.005.

Hautala, S.L., Riser, S.C., 1993. A nonconservative β-spiral determination of the deep circulation in the Eastern South Pacific. J. Phys. Oceanogr. http://dx.doi.org/10.1175/1520-0485(1993)023<1975:ANSDOT>2.0.CO;2.

Hayes, C.T., Anderson, R.F., Fleisher, M.Q., Serno, S., Winckler, G., Gersonde, R., 2013a. Quantifying lithogenic inputs to the North Pacific Ocean using the long-lived thorium isotopes. Earth Planet. Sci. Lett. 383, 16–25. http://dx.doi.org/10.1016/j.epsl.2013.09.025.

Hayes, C.T., Anderson, R.F., Jaccard, S.L., Francois, R., Fleisher, M.Q., Soon, M., Gersonde, R., 2013b. A new perspective on boundary scavenging in the North Pacific Ocean. Earth Planet. Sci. Lett. 369–370, 86–97. http://dx.doi.org/10.1016/j.epsl.2013.03.008.

Hayes, C.T., Anderson, R.F., Fleisher, M.Q., Huang, K.-F., Robinson, L.F., Lu, Y., Cheng, H., Edwards, R.L., Moran, S.B., 2015a. 230Th and 231Pa on GEOTRACES GA03, the U.S. GEOTRACES North Atlantic transect, and implications for modern and paleoceanographic chemical fluxes. Deep-Sea Res. II Top. Stud. Oceanogr. 116, 29–41. http://dx.doi.org/10.1016/j.dsr2.2014.07.007.

Hayes, C.T., Anderson, R.F., Fleisher, M.Q., Vivancos, S.M., Lam, P.J., Ohnemus, D.C., Huang, K.-F., Robinson, L.F., Lu, Y., Cheng, H., Edwards, R.L., Moran, S.B., 2015b. Intensity of Th and Pa scavenging partitioned by particle chemistry in the North Atlantic Ocean. Mar. Chem. 170, 49–60. http://dx.doi.org/10.1016/j.marchem.2015.01.006.

Hayes, C.T., Fitzsimmons, J.N., Boyle, E.A., McGee, D., Anderson, R.F., Weisend, R., Morton, P.L., 2015c. Thorium isotopes tracing the iron cycle at the Hawaii Ocean Time-series Station ALOHA. Geochim. Cosmochim. Acta 169, 1–16. http://dx.doi.org/10.1016/j.gca.2015.07.019.

Hayes, C.T., Rosen, J., McGee, D., Boyle, E.A., 2017. Thorium distributions in high- and low-dust regions and the significance for iron supply. Glob. Biogeochem. Cycles 31, 328–347. http://dx.doi.org/10.1002/2016GB005511.

Henderson, G.M., Anderson, R.F., 2003. The U-series toolbox for paleoceanography. Rev. Mineral. Geochem. 52 (1), 493–531.

Henderson, G.M., Heinze, C., Anderson, R.F., Winguth, A.M.E., 1999. Global distribution of the flux to ocean sediments constrained by GCM modelling. Deep-Sea Res. I Oceanogr. Res. Pap. 46, 1861–1893. http://dx.doi.org/10.1016/S0967-0637(99)00030-8.

Honeyman, B.D., Balistrieri, L.S., Murray, J.W., 1988. Oceanic trace metal scavenging: the importance of particle concentration. Deep Sea Research Part. Oceanogr. Res. Pap. 35, 227–246. http://dx.doi.org/10.1016/0198-0149(88)90038-6.

Jenkins, W.J., Lott, D., German, C., Cahill, K., Goudreau, J., Longworth, B., 2017. The deep distributions of helium isotopes, radiocarbon, and noble gases along the U.S. GEOTRACES East Pacific Zonal Transect (GP16). Mar. Chem (this issue).

Jickells, T.D., An, Z.S., Andersen, K.K., Baker, A.R., Bergametti, G., Brooks, N., Cao, J.J., Boyd, P.W., Duce, R.A., Hunter, K.A., Kawahata, H., Kubilay, N., LaRoche, J., Liss, P.S., Mahowald, N., Prospero, J.M., Ridgwell, A.J., Tegen, I., Torres, R., 2005. Global iron connections between desert dust, ocean biogeochemistry, and climate. Science 308, 67–71. http://dx.doi.org/10.1126/science.1105959.

Johnson, G.C., Talley, L.D., 1997. Deep tracer and dynamical plumes in the tropical Pacific Ocean. J. Geophys. Res. Oceans 102, 24953–24964. http://dx.doi.org/10.1029/97JC01913.

Kadko, D., 1996. Radioisotopic studies of submarine hydrothermal vents. Rev. Geophys. 34, 349–366. http://dx.doi.org/10.1029/96RG01762.

Kadko, D., Feely, R., Massoth, G., 1994. Scavenging of 234Th and phosphorus removal from the hydrothermal effluent plume over the North Cleft segment of the Juan de Fuca Ridge. J. Geophys. Res. Oceans 99, 5017–5024. http://dx.doi.org/10.1029/93JB02952.

Kienast, S.S., Winckler, G., Lippold, J., Albani, S., Mahowald, N.M., 2016. Tracing dust input to the global ocean using thorium isotopes in marine sediments: ThoroMap. Glob. Biogeochem. Cycles 30, 1526–1541. http://dx.doi.org/10.1002/2016GB005408.

Kipp, L.E., Sanial, V., Henderson, P., van Beek, P., Reyss, J., Hammond, D., Moore, W., Charette, M., 2017. Radium isotopes as tracers of hydrothermal inputs and neutrally buoyant plume dynamics in the deep ocean. Mar. Chem (this issue).

Kleint, C., Hawkes, J.A., Sander, S.G., Koschinsky, A., 2016. Voltammetric investigation of hydrothermal iron speciation. Front. Mar. Sci. 3, 60. http://dx.doi.org/10.3389/fmars.2016.00075.

Klinkhammer, G., Bender, M., Weiss, R.F., 1977. Hydrothermal manganese in the Galapagos Rift. Nature 269, 319–320. http://dx.doi.org/10.1038/269319a0.

Kretschmer, S., Geibert, W., Rutgers van der Loeff, M.M., Schnabel, C., Xu, S., Mollenhauer, G., 2011. Fractionation of 230Th, 231Pa, and 10Be induced by particle size and composition within an opal-rich sediment of the Atlantic Southern Ocean. Geochim. Cosmochim. Acta 75, 6971–6987. http://dx.doi.org/10.1016/j.gca.2011.09.012.

Lam, P.J., Ohnemus, D.C., Auro, M.E., 2015. Size-fractionated major particle composition and concentrations from the US GEOTRACES North Atlantic Zonal Transect. Deep-Sea Res. II Top. Stud. Oceanogr. 116, 303–320. http://dx.doi.org/10.1016/j.dsr2.2014.11.020.

Lam, P.J., Lee, J., Heller, M., Mehic, S., Xiang, Y., Bates, N., 2017. Size-fractionated distributions of suspended particle concentration and major phase composition from the U.S. GEOTRACES Eastern Pacific Zonal Transect (GP16). Mar. Chem (this issue).

Lee, J., Heller, M., Lam, P., 2017. Size distribution of particulate trace elements in the U.S. GEOTRACES Eastern Pacific Zonal Transect (GP16). Mar. Chem (this issue).

Lerner, P., Marchal, O., Lam, P.J., Anderson, R.F., Buesseler, K., Charette, M.A., Edwards, R.L., Hayes, C.T., Huang, K.-F., Lu, Y., Robinson, L.F., Solow, A., 2016. Testing models of thorium and particle cycling in the ocean using data from station GT11-22 of the U.S. GEOTRACES North Atlantic section. Deep-Sea Res. I Oceanogr. Res. Pap. 113, 57–79. http://dx.doi.org/10.1016/j.dsr.2016.03.008.

Lerner, P., Marchal, O., Lam, P., Buesseler, K., Charette, M., 2017. Kinetics of thorium and particle cycling along the U.S. GEOTRACES North Atlantic Transect. Deep-Sea Res. I Oceanogr. Res. Pap. 125, 106–128. http://dx.doi.org/10.1016/j.dsr.2017.05.003.

Lopez, G.I., Marcantonio, F., Lyle, M., Lynch-Stieglitz, J., 2015. Dissolved and particulate 230Th–232Th in the Central Equatorial Pacific Ocean: evidence for far-field transport of the East Pacific Rise hydrothermal plume. Earth Planet. Sci. Lett. 431, 87–95. http://dx.doi.org/10.1016/j.epsl.2015.09.019.

Lund, D.C., Asimow, P.D., 2011. Does sea level influence mid-ocean ridge magmatism on Milankovitch timescales? Geochem. Geophys. Geosyst. 12. http://dx.doi.org/10.1029/2011GC003693.

Lupton, J.E., Craig, H., 1981. A major helium-3 source at 15˚S on the East Pacific Rise. Science 214, 13–18. http://dx.doi.org/10.1126/science.214.4516.13.

McGee, D., Winckler, G., Borunda, A., Serno, S., Anderson, R.F., Recasens, C., Bory, A., Gaiero, D., Jaccard, S.L., Kaplan, M., McManus, J.F., Revel, M., Sun, Y., 2016. Tracking eolian dust with helium and thorium: impacts of grain size and provenance. Geochim. Cosmochim. Acta 175, 47–67. http://dx.doi.org/10.1016/j.gca.2015.11.023.

Michard, A., Albarède, F., 1985. Hydrothermal uranium uptake at ridge crests. Nature 317, 244–246. http://dx.doi.org/10.1038/317244a0.

Misumi, K., Lindsay, K., Moore, J.K., Doney, S.C., Tsumune, D., Yoshida, Y., 2013. Humic substances may control dissolved iron distributions in the global ocean: implications from numerical simulations. Glob. Biogeochem. Cycles 27, 450–462. http://dx.doi.org/10.1002/gbc.20039.

Mottl, M.J., McConachy, T.F., 1990. Chemical processes in buoyant hydrothermal plumes on the East Pacific Rise near 21˚N. Geochim. Cosmochim. Acta 54, 1911–1927. http://dx.doi.org/10.1016/0016-7037(90)90261-I.

Murnane, R.J., Cochran, J.K., Sarmiento, J.L., 1994. Estimates of particle- and thorium-cycling rates in the northwest Atlantic Ocean. J. Geophys. Res. Oceans 99, 3373–3392. http://dx.doi.org/10.1029/93JC02378.

Okubo, A., Obata, H., Gamo, T., Yamada, M., 2012. 230Th and 232Th distributions in mid-latitudes of the North Pacific Ocean: effect of bottom scavenging. Earth Planet. Sci. Lett. 339–340, 139–150. http://dx.doi.org/10.1016/j.epsl.2012.05.012.

Reid, J.L., 1986. On the total geostrophic circulation of the South Pacific Ocean: flow patterns, tracers and transports. Prog. Oceanogr. 16, 1–61. http://dx.doi.org/10.1016/0079-6611(86)90036-4.

Resing, J.A., Sedwick, P.N., German, C.R., Jenkins, W.J., Moffett, J.W., Sohst, B.M., Tagliabue, A., 2015. Basin-scale transport of hydrothermal dissolved metals across the South Pacific Ocean. Nature 523, 200–203. http://dx.doi.org/10.1038/nature14577.

Robert, J., Miranda, C.F., Muxart, R., 1969. Mesure de la période du protactinium 231 par microcalorimétrie. Radiochim. Acta 11, 104–108. http://dx.doi.org/10.1524/ract.1969.11.2.104.

Roshan, S., Wu, J., Jenkins, W.J., 2016. Long-range transport of hydrothermal dissolved Zn in the tropical South Pacific. Mar. Chem. 183, 25–32. http://dx.doi.org/10.1016/j.marchem.2016.05.005.

Roy-Barman, M., Coppola, L., Souhaut, M., 2002. Thorium isotopes in the western Mediterranean Sea: an insight into the marine particle dynamics. Earth Planet. Sci. Lett. 196, 161–174. http://dx.doi.org/10.1016/S0012-821X(01)00606-9.

Roy-Barman, M., Lemaître, C., Ayrault, S., Jeandel, C., Souhaut, M., Miquel, J.C., 2009. The influence of particle composition on Thorium scavenging in the Mediterranean

Sea. Earth Planet. Sci. Lett. 286, 526–534. http://dx.doi.org/10.1016/j.epsl.2009.07.018.

Rudnicki, M.D., Elderfield, H., 1993. A chemical model of the buoyant and neutrally buoyant plume above the TAG vent field, 26 degrees N, Mid-Atlantic Ridge. Geochim. Cosmochim. Acta 57, 2939–2957. http://dx.doi.org/10.1016/0016-7037(93)90285-5.

Rutgers van der Loeff, M.M., Meyer, R., Rudels, B., Rachor, E., 2002. Resuspension and particle transport in the benthic nepheloid layer in and near Fram Strait in relation to faunal abundances and 234Th depletion. Deep-Sea Res. I Oceanogr. Res. Pap. 49, 1941–1958. http://dx.doi.org/10.1016/S0967-0637(02)00113-9.

Saito, M.A., Noble, A.E., Tagliabue, A., Goepfert, T.J., Lamborg, C.H., Jenkins, W.J., 2013. Slow-spreading submarine ridges in the South Atlantic as a significant oceanic iron source. Nat. Geosci. 6, 775–779. http://dx.doi.org/10.1038/ngeo1893.

Sander, S.G., Koschinsky, A., 2011. Metal flux from hydrothermal vents increased by organic complexation. Nat. Geosci. 4, 145–150. http://dx.doi.org/10.1038/ngeo1088.

Schlitzer, R., 2016. Quantifying He fluxes from the mantle using multi-tracer data assimilation. Philos. Trans. A Math. Phys. Eng. Sci. 374, 20150288. http://dx.doi.org/10.1098/rsta.2015.0288.

Shen, C.-C., Lawrence Edwards, R., Cheng, H., Dorale, J.A., Thomas, R.B., Bradley Moran, S., Weinstein, S.E., Edmonds, H.N., 2002. Uranium and thorium isotopic and concentration measurements by magnetic sector inductively coupled plasma mass spectrometry. Chem. Geol. 185, 165–178. http://dx.doi.org/10.1016/S0009-2541(01)00404-1.

Shen, C.C., Cheng, H., Edwards, R.L., Moran, S.B., 2003. Measurement of attogram quantities of 231Pa in dissolved and particulate fractions of seawater by isotope dilution thermal ionization mass spectroscopy. Anal. Chem. http://dx.doi.org/10.1021/ac026247r.

Shen, C.-C., Wu, C.-C., Cheng, H., Lawrence Edwards, R., Hsieh, Y.-T., Gallet, S., Chang, C.-C., Li, T.-Y., Lam, D.D., Kano, A., Hori, M., Spötl, C., 2012. High-precision and high-resolution carbonate 230Th dating by MC-ICP-MS with SEM protocols. Geochim. Cosmochim. Acta 99, 71–86. http://dx.doi.org/10.1016/j.gca.2012.09.018.

Shimmield, G.B., Price, N.B., 1988. The scavenging of U,230Th and 231Pa during pulsed hydrothermal activity at 20˚S, East Pacific Rise. Geochim. Cosmochim. Acta 52, 669–677. http://dx.doi.org/10.1016/0016-7037(88)90329-8.

Stommel, H., 1982. Is the South Pacific helium-3 plume dynamically active? Earth Planet. Sci. Lett. 61, 63–67. http://dx.doi.org/10.1016/0012-821X(82)90038-3.

Tagliabue, A., Resing, J., 2016. Impact of hydrothermalism on the ocean iron cycle. Philos. Trans. A Math. Phys. Eng. Sci. 374, 20150291. http://dx.doi.org/10.1098/rsta.2015.0291.

Tagliabue, A., Bopp, L., Dutay, J.-C., Bowie, A.R., Chever, F., Jean-Baptiste, P., Bucciarelli, E., Lannuzel, D., Remenyi, T., Sarthou, G., Aumont, O., Gehlen, M., Jeandel, C., 2010. Hydrothermal contribution to the oceanic dissolved iron inventory. Nat. Geosci. 3, 252–256. http://dx.doi.org/10.1038/ngeo818.

Tagliabue, A., Aumont, O., Bopp, L., 2014. The impact of different external sources of iron on the global carbon cycle. Geophys. Res. Lett. 41, 920–926. http://dx.doi.org/10.1002/2013GL059059.

Thurnherr, A.M., Richards, K.J., German, C.R., Speer, K.G., 2002. Flow and mixing in the rift valley of the Mid-Atlantic Ridge. JPO. http://dx.doi.org/10.1175/1520-0485(2002)032<1763:FAMITR>2.0.CO;2.

Toner, B.M., Fakra, S.C., Manganini, S.J., Santelli, C.M., Marcus, M.A., Moffett, J.W., Rouxel, O., German, C.R., Edwards, K.J., 2009. Preservation of iron(II) by carbon-rich matrices in a hydrothermal plume. Nat. Geosci. 2, 197–201. http://dx.doi.org/10.1038/ngeo433.

Toner, B.M., Marcus, M.A., Edwards, K.J., Rouxel, O.J., German, C.R., 2012. Measuring the Form of Iron in Hydrothermal Plume Particles. http://dx.doi.org/10.5670/oceanog.2012.19.

Trocine, R.P., Trefry, J.H., 1988. Distribution and chemistry of suspended particles from an active hydrothermal vent site on the Mid-Atlantic Ridge at 26˚N. Earth Planet. Sci. Lett. 88, 1–15. http://dx.doi.org/10.1016/0012-821X(88)90041-6.

Völker, C., Tagliabue, A., 2015. Modeling organic iron-binding ligands in a three-dimensional biogeochemical ocean model. Mar. Chem. 173, 67–77. http://dx.doi.org/10.1016/j.marchem.2014.11.008.

Von Damm, K.L., Edmond, J.M., Grant, B., Measures, C.I., Walden, B., Weiss, R.F., 1985. Chemistry of submarine hydrothermal solutions at 21 ˚N, East Pacific Rise. Geochim. Cosmochim. Acta 49, 2197–2220. http://dx.doi.org/10.1016/0016-7037(85)90222-4.

Yücel, M., Luther, G.W., 2013. Temporal trends in vent fluid iron and sulfide chemistry following the 2005/2006 eruption at East Pacific Rise, 9˚50′N. Geochem. Geophys. Geosyst. 14, 759–765. http://dx.doi.org/10.1002/ggge.20088.